

Dense Forests of Microshots in Bursts from FRB 20220912A

Danté M. Hewitt,^{1*} Jason W. T. Hessels,^{1,2} Omar S. Ould-Boukattine,^{2,1} Pragya Chawla,¹ Ismaël Cognard,^{3,4} Akshatha Gopinath,¹ Lucas Guillemot,^{3,4} Daniela Huppenkothen,^{5,1} Kenzie Nimmo⁶ and Mark P. Snelders^{2,1}

¹*Anton Pannekoek Institute for Astronomy, University of Amsterdam, Science Park 904, 1098 XH, Amsterdam, The Netherlands*

²*ASTRON, Netherlands Institute for Radio Astronomy, Oude Hoogeveensedijk 4, 7991 PD Dwingeloo, The Netherlands*

³*Station de Radioastronomie de Nançay, Observatoire de Paris, PSL University, CNRS, Université d'Orléans, F-18330 Nançay, France*

⁴*Laboratoire de Physique et Chimie de l'Environnement et de l'Espace LPC2E UMR7328, Université d'Orléans, CNRS, F-45071 Orléans, France*

⁵*SRON Netherlands Institute for Space Research, Niels Bohrweg 4, 2333 CA, Leiden, Netherlands*

⁶*MIT Kavli Institute for Astrophysics and Space Research, Massachusetts Institute of Technology, 77 Massachusetts Ave, Cambridge, MA 02139, USA*

Accepted XXX. Received YYY; in original form ZZZ

ABSTRACT

We report on exceptionally bright bursts (>400 Jy ms) detected from the repeating fast radio burst source FRB 20220912A using the Nançay Radio Telescope (NRT), as part of the ECLAT (Extragalactic Coherent Light from Astrophysical Transients) monitoring campaign. These bursts exhibit extremely luminous, broadband, short-duration structures (~ 16 μ s), which we term ‘microshots’ and which can be especially well studied in the NRT data given the excellent signal-to-noise and dynamic range (32-bit samples). The estimated peak flux density of the brightest microshot is 450 Jy. We show that the microshots are clustered into dense ‘forests’, by modelling them as Weibull distributions and obtaining Weibull shape parameters of approximately 0.5. Our polarimetric analysis reveals that the bursts are nearly 100% linearly polarised; have $\lesssim 10$ % circular polarisation fractions; a near-zero average rotation measure of $0.10(6)$ rad m^{-2} ; and varying polarisation position angles over the burst duration. For one of the bursts, we analyse raw voltage data from simultaneous observations with the Westerbork RT-1 single 25-m dish. These data allow us to measure the scintillation bandwidth, $0.30(3)$ MHz, and to probe the bursts on (sub-)microsecond timescales. Some important nuances related to dedispersion are also discussed. We propose that the emission mechanism for the broadband microshots is potentially different from the emission mechanism of the broader burst components which still show a residual drift of a few hundred MHz ms^{-1} after correcting for dispersion using the microshots. We discuss how the observed emission is phenomenologically analogous to different types of radio bursts from the Sun.

Key words: fast radio bursts – radio continuum: transients

1 INTRODUCTION

Fast radio bursts (FRBs) are coherent radio transients, typically lasting a few milliseconds. Their extragalactic origin was inferred from their excess dispersion measures (DMs) and has been confirmed by multiple localisations to a diverse set of host galaxies (for a recent review of FRBs, see Petroff et al. 2022). A small fraction (~ 2.6 %; Chime/Frb Collaboration et al. 2023) of known FRBs are confirmed repeaters (Spitler et al. 2016) that emit multiple bursts — more often than not, sporadically and infrequently. These repeater bursts are, on average, longer in duration and narrower in observed emission bandwidth compared to the apparently non-repeating FRBs (Pleunis et al. 2021). Conversely, it has recently been demonstrated that the repetition rates of repeaters and the upper limits on repetition from apparently non-repeaters are not clearly distinct, after exposure and sensitivity corrections (Chime/Frb Collaboration et al. 2023). There are, however, some anomalously prolific repeaters that have appeared to suddenly awaken from quiescence, e.g., FRB 20201124A (Chime/Frb Collaboration 2021). A non-negligible fraction of apparently non-repeating sources may thus in fact be repeaters (either

with low repetition rates or long periods of quiescence); if so, their shorter-duration and wider-bandwidth bursts could arise from a different emission mechanism and/or beaming effects (Connor et al. 2020).

Many theories advocate for highly magnetized neutron stars as the progenitors of FRBs. This hypothesis has been strengthened by the detection of an extremely bright, millisecond-duration radio burst from the Galactic magnetar SGR 1935+2154 (Bochenek et al. 2020; CHIME/FRB Collaboration et al. 2020). It is presently unclear whether the repeating and apparently non-repeating FRBs originate from the same progenitor(s). So far, there also seems to be no distinction in the properties of the host galaxies of repeaters and apparent non-repeaters (Bhandari et al. 2022; Gordon et al. 2023). If assuming a universal magnetar progenitor, however, different formation channels are required in order to reconcile the rate of all extragalactic FRBs with the volumetric population of magnetars (Margalit et al. 2020; Kirsten et al. 2022a).

The repeater population itself, also boasts rich diversity. Repeaters have been localised to various types of host galaxies, including dwarf galaxies (e.g., FRB 20121102A and FRB 20190520B, Chatterjee et al. 2017; Niu et al. 2022), spiral galaxies (e.g., FRB 20180916B, Marcote et al. 2020) and even a globular cluster in the nearby M81

* E-mail: d.m.hewitt@uva.nl

galactic system (Kirsten et al. 2022a). Furthermore, the propagation effects we can measure from bursts such as scattering times, Faraday rotation measure (RM), and DM (as well as the evolution of these properties) suggest diverse, yet quite often chaotic, magneto-ionic local environments for the repeaters (e.g., Michilli et al. 2018; McKimven et al. 2023). There are various other characteristics that can be used to group repeaters: FRB 20121102A and FRB 20190520B are the only repeaters so far associated with a persistent radio source (Chatterjee et al. 2017; Marcote et al. 2017; Niu et al. 2022), potentially a nebula powered by the FRB source; FRB 20121102A and FRB 20180916B are the only repeaters so far that show an underlying periodicity in their activity windows (of ~ 16 and ~ 160 days, respectively; Chime/Frb Collaboration et al. 2020; Rajwade et al. 2020; Cruces et al. 2021); FRB 20180916B and FRB 20200120E are the only repeaters so far that exhibit (sub-)microsecond burst structure (Nimmo et al. 2021, 2022); and only a handful of repeaters are known to enter periods of high activity (‘burst storms’, e.g., Li et al. 2021; Hewitt et al. 2022; Zhou et al. 2022; Nimmo et al. 2023). It is thus also unclear whether all repeaters originate from the same progenitor(s). The relationship between the various FRB sources we observe is clearly intricate, but detailed studies of burst properties can help further our understanding.

On 15 October 2022, the CHIME/FRB Collaboration announced that a new repeating FRB source, FRB 20220912A had become active. Within 3 days (with a daily exposure time of only $\approx 10 - 15$ minutes) CHIME/FRB detected 9 bursts from this source at 400 – 800 MHz and report a DM of $219.46 \text{ pc cm}^{-3}$ (McKinven & Chime/Frb Collaboration 2022). FRB 20220912A has since proven to be one of the most active known repeaters to date. The vast majority of the bursts have been detected around ~ 1.4 GHz (L-band), where multiple telescopes, including the 100-m Green Bank Telescope (GBT), Five hundred meter Aperture Spherical Telescope (FAST), and Effelsberg 100-m telescope have detected more than a hundred bursts within a few hours or less of observations (e.g., Feng et al. 2022; Zhang et al. 2022; Kirsten et al. 2022b; Feng et al. 2023; Zhang et al. 2023). Bursts have also been detected at lower frequencies ($\sim 300 - 400$ MHz; Bhusare et al. 2022; Ould-Boukattine et al. 2022) and at higher frequencies around 2 GHz (S-band; Perera et al. 2022; Rajwade et al. 2022). Thus far, however, no bursts have been detected above 3 GHz despite many hours of observations (Kirsten et al. 2022b; Rajwade et al. 2022; Sheikh et al. 2022), or at the operating frequencies of the LOFAR High-Band Antennas where other repeaters have been seen (110-190 MHz; Gopinath et al. 2023).

The majority of repeaters exhibit high fractions of linear polarisation, and little to no circular polarisation (e.g., Gajjar et al. 2018; Day et al. 2020; Nimmo et al. 2021). The brightest burst detected from FRB 20220912A by CHIME/FRB (~ 600 MHz), also exhibited 100% linear polarisation, and showed an RM value of¹ $+0.6(1) \text{ rad m}^{-2}$ (McKinven & Chime/Frb Collaboration 2022). Bursts detected at higher frequencies (~ 1.4 GHz) from FAST and the GBT show similar properties: 100% linear polarisation and relatively stable RM values close to zero rad m^{-2} , the latter being indicative of a clean local environment. Additionally, approximately half of the bursts have some degree of circular polarisation, making FRB 20220912A the repeater with the highest known fraction of bursts that exhibit circular polarisation (Feng et al. 2023; Zhang et al. 2023). Furthermore, some bursts have polarisation position angle (PPA) swings, which is also scarce among the known repeaters (see Luo et al. 2020).

FRB 20220912A was localised to a host galaxy with redshift $z = 0.0771(1)$ by the Deep Synoptic Array (DSA-110) during its commissioning phase (Ravi et al. 2023). The host, PSO J347.2702+48.70, is a massive galaxy ($\log M_* = 10.0(1)$) with moderate star formation ($\text{SFR} \gtrsim 0.1 M_\odot \text{ yr}^{-1}$), not unlike other FRB host galaxies (Gordon et al. 2023). The host galaxy is located at a luminosity distance of $362.4(1) \text{ Mpc}$ and classified as composite in the Baldwin, Phillips & Terlevich (BPT) scheme.

In this paper, we present three exceptionally bright bursts detected from FRB 20220912A using the Nançay Radio Telescope (NRT). For two of the bursts, we have simultaneous coverage with the Westerbork RT-1 single 25-m dish, which recorded raw voltage data, allowing us to study burst properties at the Nyquist limit, but with lower bandwidth and sensitivity compared to NRT. The excellent quality of these combined data, together with the extraordinary signal-to-noise (S/N) of the bursts, provide a great opportunity for an in-depth study of burst features. In Section 2 we describe the observational setup and data acquisition. In Section 3 we describe our search for bursts and the analysis used to investigate the burst properties. In Section 4 we discuss the challenges related to determining an accurate DM. This is critical for the subsequent discussion where we probe the range of timescales of the emission in these bursts from FRB 20220912A and provide observational evidence that FRBs can contain short timescale (and sometimes narrow-band) shots of emission that are tightly packed together. We then compare our findings with what is seen from other FRBs, pulsar giant pulses, magnetar bursts, and solar radio bursts. Finally, in Section 5 we conclude and put forward some recommendations for future work. Throughout the paper, unless otherwise mentioned, numbers in parentheses of our measurements are used to indicate the 3σ -uncertainty on the least significant digits.

2 OBSERVATIONS

2.1 Nançay Radio Telescope

The NRT is a Kraus type meridian telescope situated in the centre of France. At ~ 1.4 GHz the NRT has a system temperature of $T_{\text{sys}} \approx 35 \text{ K}$ and a gain of $G \approx 1.4 \text{ K/Jy}$, making it effectively as sensitive as a 100-m radio dish. At the beginning of 2022 we established a monitoring campaign called ECLAT² (Extragalactic Coherent Light from Astrophysical Transients; PI: D. M. Hewitt) on the NRT. ECLAT is conducting follow-up observations of about a dozen repeaters with approximate weekly cadence over the course of two years. Thus far, bursts have been detected from more than half of the sources, establishing the NRT as a valuable instrument for FRB research. Following the detection of FRB 20220912A by CHIME/FRB we included this source among the repeaters that are regularly monitored. The pointing position we used was that of the original DSA-110 localisation: RA= $23^{\text{h}}09^{\text{m}}05.49^{\text{s}}$ Dec= $+48^\circ 42' 25.6''$ (J2000; Ravi 2022). The offset from the final localization: RA= $23^{\text{h}}09^{\text{m}}04.9^{\text{s}}$ Dec= $+48^\circ 42' 25.4''$ (J2000; Ravi et al. 2023) is $5.8''$ but this does not impact our observations as the NRT has a half-power beam width of $4' \text{ (RA)} \times 22' \text{ (Dec)}$ at 1.4 GHz.

These data were acquired using the Low Frequency receiver (1.1 – 1.8 GHz) of the focal plane and receivers systems called FORT (*Foyer Optimisé pour le Radio Télescope*), and have 512 MHz of bandwidth (consisting of 128 channels) centered at a frequency of 1484 MHz. The data were recorded as 8 subbands, each consisting of

¹ Note that, when convenient, we use parentheses to indicate the uncertainty on the least significant digits.

² *Éclat* can be translated as ‘burst’ in French.

sixteen 4-MHz channels, using the Nançay Ultimate Pulsar Processing Instrument (NUPPI; [Desvignes et al. 2011](#)) with a time resolution of $16 \mu\text{s}$, 32-bit sampling (which is better than most FRB observations and hence provides excellent dynamic range for studying these bursts) and full polarisation information in a linear basis. Coherent dedispersion, within the 4-MHz channels, was applied using a DM of $219.46 \text{ pc cm}^{-3}$ for FRB 20220912A, as reported by [McKinven & Chime/Frb Collaboration \(2022\)](#). The maximum DM offset that corresponds to a temporal smearing equal to the time resolution of the NRT data is 0.9 pc cm^{-3} . We measure DMs for the detected bursts with a smaller offset than this and consequently, the residual temporal smearing due to inaccurate coherent dedispersion, even in the worst case scenario, is still less than half the NRT sampling time (DM determination is discussed further in Section 3.2). Additionally, each observation is accompanied by an observation of a 3-Hz pulsed noise diode, which is used to calibrate the polarimetry.

2.2 Westerbork RT-1

We were also monitoring FRB 20220912A during this period using a single 25-m Westerbork dish (RT-1) in the Netherlands. The SEFD³ at 1.4 GHz is 420 Jy. The Westerbork observations were conducted with an observing bandwidth of 128 MHz centered at 1271 MHz. Raw voltage data were recorded as 2-bit samples of both left and right circular polarisations with the local DBBC2 and Flexbuff systems, and stored in VLBI Data Interchange Format (VDIF; [Whitney et al. 2010](#)). Using `digi.fil` from the standard pulsar software package DSPSR ([van Straten & Bailes 2011](#)), we created Stokes I filterbanks from the voltage data, with frequency and time resolutions of 62.5 kHz and $64 \mu\text{s}$, respectively, which we then used to search for bursts. We also created filterbank data products from the raw voltages at the time of detected bursts, with different time/frequency resolution combinations, for other analyses, as will be explained in later sections.

3 ANALYSIS AND RESULTS

3.1 Burst search

3.1.1 The ECLAT burst search pipeline

NUPPI records data as eight 64-MHz subbands, which we stitch together and write out as 32-bit Stokes I filterbanks with 512-MHz bandwidth using custom Python scripts that incorporate functionality from the YOUR (Your Unified Reader) library ([Aggarwal et al. 2020b](#)). These filterbanks are converted to 8-bit samples using `digi.fil` for compatibility with the `Heimdal1` software used later in the pipeline. The 8-bit filterbanks are then processed in two-minute chunks using the `rfi.find` tool from the PRESTO pulsar software suite ([Ransom 2001](#)), to determine which channels are most contaminated by radio frequency interference (RFI). We flag only these channels and apply no flagging to individual time intervals. The flagged data are then searched using `Heimdal1`, where we set a S/N threshold of 7. We effectively searched for boxcar widths ranging from $16 \mu\text{s}$ to 131 ms within a DM range of $200\text{--}250 \text{ pc cm}^{-3}$ for FRB 20220912A. Candidates from the `Heimdal1` search are classified by the machine-learning classifier FETCH ([Aggarwal et al. 2020a](#)). We manually inspect all the candidates for which any of the FETCH models A to H give a score above 0.5. If the bursts pass this manual inspection and

are considered astrophysical, they are extracted from the original 32-bit data with full polarisation information. The 32-bit data are used for the remainder of the analyses.

We detected many hundreds of bursts from FRB 20220912A, and while the burst rate drastically decreased around the end of 2022, we are still occasionally detecting bursts at the time of writing this manuscript. The entire burst sample and a study of the evolution of the burst properties over time will be presented in a future paper. On 29 October 2022 (MJD 59881), 1 November 2022 (MJD 59884), and 16 November 2022 (MJD 59899), we detected exceptionally bright bursts from FRB 20220912A, which we refer to as B1, B2 and B3, respectively, throughout the rest of this paper. These were the three bursts with the highest detection S/N.

In Figure 1, we show the dynamic spectra, frequency-averaged burst profiles, and time-averaged spectra of the three brightest bursts detected thus far from FRB 20220912A in our ECLAT observations. Each frequency channel in the dynamic spectrum has been individually normalised using off-burst statistics (i.e., bandpass corrected). The brightness variations in the spectra that are a few bins wide are likely the result of unresolved scintillation. The extreme S/N of these bursts results in some artifacts from out-of-band emission before the first digitisation stage that can be seen in the dynamic spectra at the highest observed frequencies, before the burst occurs.

Two of the three bright bursts exhibit clustered broadband (and sometimes exquisitely bright) emission components that are sometimes a single $16\text{-}\mu\text{s}$ time bin in duration. Throughout this paper we refer to these extremely short-timescale, broadband structures as ‘microshots’. In Figure 2 the top panels show the time profile of the entire burst envelopes, while the middle and bottom panels display zoom-ins of the time profiles and dynamic spectra where the microshots appear. In the middle panels we have also over-plotted, in purple, the time profile on a logarithmic scale y-axis, which reveals many more microshots that are less apparent in the linear scale. The microshots have been manually identified and are indicated by vertical turquoise lines in the figure.

3.1.2 Westerbork burst search

The burst search pipeline used to search the Westerbork data has been previously described in detail ([Kirsten et al. 2021, 2022a](#)). Westerbork was not on source during burst B1, but on 29 October 2022 and 16 November 2022 the ECLAT observations overlapped with Westerbork observations and B2 and B3 were independently discovered in the search of the Westerbork data.

3.2 Dispersion Measure determination

We determined the DM of B1 using the three extremely bright and broadband microshots seen in the dynamic spectrum of the NRT data. We chose a DM that ensured that these microshots each individually arrive at all observed frequencies at the same time. This was done by dedispersing these three microshots to a range of trial DM values using a technique that shifts channels by fractions of a bin. We then fitted a Gaussian to these S/N versus DM curves to determine an optimal value and uncertainty. The microshots slightly differ from one another in their skewness, brightness, duration and bandwidth. Together with the intense variations in brightness as a function of frequency (likely scintillation, as we discuss later) this complicates the DM determination, but we attempt to mitigate this by averaging the power of a few microshots, and fitting a Gaussian to this averaged S/N vs DM curve. The resulting fits are shown in Appendix Figure A1. The curves are not smooth and exhibit scalloping that differs

³ www.evlbi.org/sites/default/files/shared/EVNstatus.txt

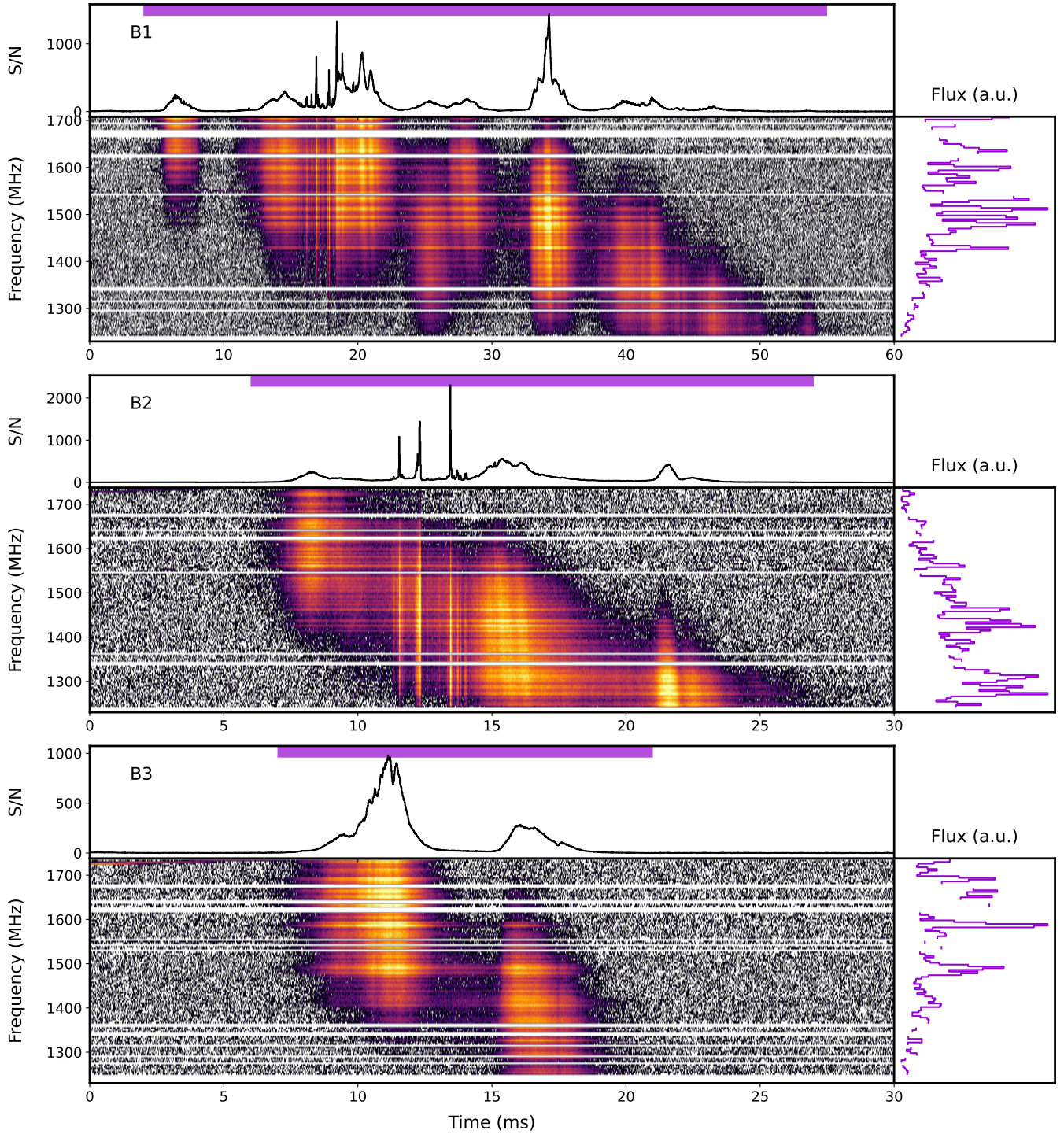


Figure 1. Dynamic spectra of three bursts detected from FRB 20220912A with the NRT as part of the ECLAT monitoring campaign. The burst IDs (see Table 1) are shown in the top-left corners of each sub-figure. The frequency and time resolution are 4 MHz and 16 μ s, respectively. In addition to being coherently dedispersed to a DM of 219.46 pc cm⁻³, bursts B1, B2 and B3 have also been incoherently dedispersed to DMs of 219.356, 219.375 and 219.8 pc cm⁻³, respectively (see the main text for more details). Horizontal white lines in the dynamic spectra indicate frequency channels that have been excised due to the presence of RFI. The top panel of each sub-figure shows the frequency-averaged time series of the burst, and the right panel shows the time-averaged spectrum of the burst. The time series is obtained by summing over the entire observing bandwidth, while the spectrum is obtained by only summing over the times where the burst is present (determined by eye and indicated by the purple bar in the top panel). The spikes in the frequency spectra are likely due to scintillation in the Galactic ISM. Note that while the frequency extent of each dynamic spectrum is the same, the time extent is not. The noise is Gaussian-distributed with a standard deviation of 1 and a mean of 0. The colour scale for all sub-figures has been logarithmically scaled using the 99.9 quantile as the maximum and a value of 1 as the minimum. Note that artifacts, arising from out-of-band emission before the first digitisation stage, are visible in the highest-frequency channels, preceding the burst.

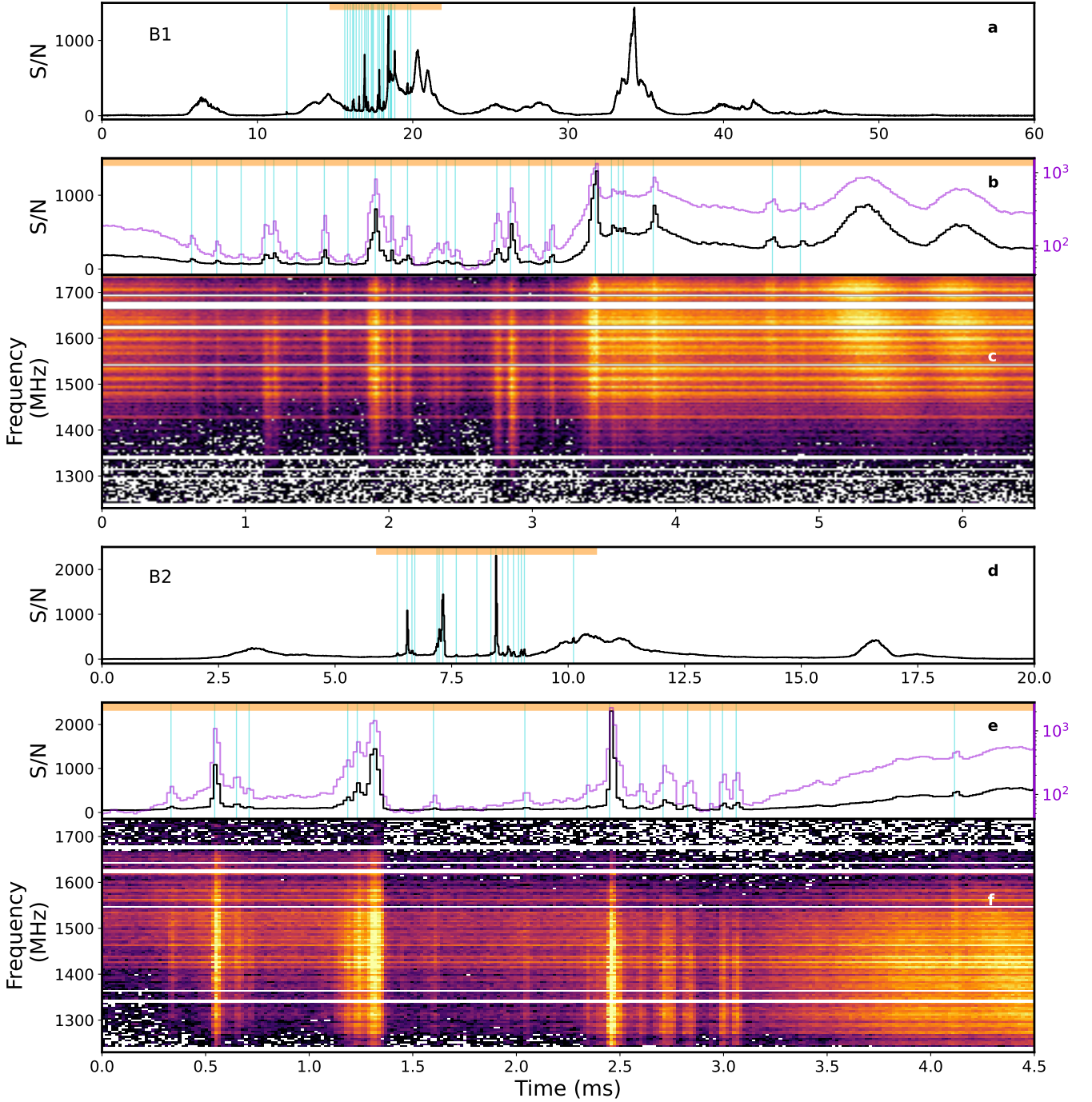


Figure 2. A zoomed-in view of bursts B1 and B2 is shown in the two sub-figures. Panels a and d show the full temporal burst profile of bursts B1 and B2, respectively. Microshots are indicated by vertical turquoise lines. In each of these panels, the time-span where the microshots are clustered is indicated by a horizontal orange bar. Panels b and e show zoom-ins of these regions. The purple profile is the same as the black, but on a logarithmic y-scale, revealing microshots that are less visible in the black linearly scaled profile due to the wide range of observed S/Ns. The dynamic spectra of these zoomed-in regions are shown in panels c and f. Horizontal white lines indicate channels that have been zapped due to the presence of RFI. Also note the residual frequency drift present in the broader burst components that occur after the microshot forests in panel c.

from one microshot to another. This occurs because the microshots have durations comparable to the time resolution of our data and our frequency resolution is rather coarse (since coherent dedispersion has been implemented beforehand). Artificially increasing the time resolution of the dynamic spectrum before dedispersion (with nearest neighbour interpolation), and then downsampling to the original time

resolution after the frequency channels have been shifted, results in slightly less scatter in S/N versus DM. In the Westerbork data, where sub-microsecond resolution is available, the scalloping disappears. Our fits yield a DM of $219.356(12) \text{ pc cm}^{-3}$ for B1. B2 similarly has three extremely bright and broadband microshots that were used to determine a DM of $219.377(9) \text{ pc cm}^{-3}$. Consistent measurements

were obtained by performing similar analysis on the Westerbork data of B2 (time resolution of $1 \mu\text{s}$). B3, however, shows no microshots, even when exploring the burst with higher time resolution in the Westerbork data. Here we thus focused on straightening the notches (narrow intensity dips) that are present in the burst, resulting in a DM of $219.8(1) \text{ pc cm}^{-3}$. This is likely a slight overestimation of the DM because the DM that straightens the microshots in the other bursts does not necessarily straighten the dips in the broader sub-bursts. For the remainder of the analyses we use the aforementioned DM values, tabulated in Table 1, unless stated otherwise.

In the literature, DMs are often determined using `DM_phase` (Seymour et al. 2019)⁴, which maximizes the coherent power of a burst across the bandwidth in order to determine a best DM. For the sake of comparison, using the entire burst as input for `DM_phase`, while applying a bandpass filter to limit the fluctuation frequencies between 1 and 15.625 ms^{-1} (i.e., timescales ranging from 2 bins to 1 ms) results in optimal DMs of $219.35(3)$, $219.37(2)$ and $219.8(2) \text{ pc cm}^{-3}$ for bursts B1, B2 and B3, respectively (1σ -uncertainties). These values are consistent with those we obtain from aligning the microshots to arrive at the same time at all observed frequencies. All the aforementioned DM values are summarised in Table 2.

Moreover, these DMs are generally consistent with what was reported by CHIME/FRB and others thus far. In Section 4.1 we further justify our decision for determining the DM in this manner and discuss other important nuances related to FRB DM determination in general.

3.3 Measurement of burst properties

Some properties of the bursts are tabulated in Table 1. Before determining any properties we first removed the bandpass: for each channel we subtract the mean and divide by the standard deviation of the off-burst noise, free of any obvious RFI. To convert these pixels, which are now in S/N units, to physical flux densities we multiply by the radiometer equation.

3.3.1 ACF analysis

We measured drift rates by calculating 2D autocorrelation functions (ACFs) of the bursts. We masked the zero-lag noise spike and then fitted a 2D Gaussian function to the ACF, following the technique detailed in Chamma et al. (2021). Uncertainties on the drift rate are calculated as in Gopinath et al. (2023). The ACFs of the bursts can be seen in Appendix Figure B1. The angle of the 2D Gaussian is defined as the orientation of the semi-major axis measured counterclockwise from the positive y-axis and the tangent of this angle gives the burst drift rates reported in Table 1. These drift rates are comparable to drift rates measured in other complex bursts from FRBs such as FRB 20201124A (e.g., Zhou et al. 2022), and with the lower-end of drifts measured for FRB 20121102A (e.g., Hessels et al. 2019). Measurement of drift rates at other radio frequency bands are necessary to determine whether the drift rate varies linearly with frequency for FRB 20220912A as it does for other repeaters (e.g., Hessels et al. 2019; Gopinath et al. 2023).

The 2D ACFs can further be used to measure the frequency and time scales of brightness variations in these bursts. The Galactic coordinates of FRB 20220912A are $l = 106.1^\circ$, $b = -10.8^\circ$; it thus lies slightly outside of the Galactic plane and scatter broadening should consequently be moderate. The expected scattering timescale

for FRB 20220912A at 1 GHz according to the NE2001 Galactic electron density model (Cordes & Lazio 2002) is $2.6 \mu\text{s}$. Assuming a frequency scaling of $\tau \propto \nu^{-4}$, the expected scattering time at the center of the Westerbork band (1.271 GHz) is $1.0 \mu\text{s}$, corresponding to a scintillation bandwidth of 160 kHz (using the approximation $\Delta\nu \sim 1/2\pi\tau$). At 1.484 GHz, which is the center of the NRT band, the scintillation bandwidth is expected to be approximately 290 kHz, which is less than a tenth of the frequency resolution of these data (4 MHz). Since the frequency resolution of our NRT data is too coarse to resolve the expected scintillation bandwidth we do not attempt to measure it in the frequency ACF. The presence of a one-bin peak at the centre of the frequency ACF, does however hint at a scintillation bandwidth of a few MHz at most. Fortunately, as previously mentioned, voltage data were recorded for B2 with Westerbork RT-1 and we were thus able to generate coherently dedispersed total intensity filterbanks with even higher time and/or frequency resolution than that of the NRT data, using the Super FX Correlator, SFXC (Keimpema et al. 2015). We constructed data products with a frequency resolution of 62.5 kHz and computed an ACF of these data, allowing us to distinguish between the different frequency scales that are present. We then fit a Lorentzian function to the narrow central feature present in the 1D frequency ACF and measure a scintillation bandwidth, defined as the half-width at half-maximum of the Lorentzian, of $300(30) \text{ kHz}$ (see Figure B2). This corresponds to a scattering timescale of $\sim 0.5 \mu\text{s}$ at 1.271 GHz, which is consistent within a factor of 2 with the prediction from NE2001. Moreover, once frequency scaling has been taken into account, our measurement is also consistent with the scintillation bandwidth of $390(20) \text{ kHz}$ reported from FAST observations that were conducted at a central frequency of 1.3 GHz (Wu et al. 2023).

3.3.2 Power spectrum analysis

In Nimmo et al. (2021, 2022) the power spectra of bursts are computed to determine if the bursts are consistent with red noise and to explore whether there are any significant features present in the power spectra such as quasi-periodic oscillations (QPOs). Following this same procedure and using the `Stingray` modelling interface (Huppenkothen et al. 2019), we computed the power spectra of bursts B1 to B3 using the NRT data, as well as B2 with the Westerbork data (which has a $16\times$ higher time resolution of $1 \mu\text{s}$), and modelled them as power laws (red noise), where the maximum-a-posteriori model is of the form:

$$f(\omega) = A\omega^\alpha + C \quad (1)$$

Here, ω is the frequency, A is the amplitude, α is the power law index and C is a white noise constant. We assume flat priors for A and α , and a normal prior for C . In the case of B1 and B2 with the NRT data, C could not be well constrained, so we only fit a power law without a white noise constant. These power law fits and residuals are shown in Figure 3. The power law indices we estimate are presented in Table 2. These values are comparable to those of FRB 20180916B and FRB 20200120E (Nimmo et al. 2021, 2022). The power laws for B1 and B2 are flatter than that of B3, which is in agreement with B1 and B2 having more significant power at higher frequencies (shorter timescales) due to the presence of microshots. Furthermore, these fits allow us to investigate the highest fluctuation frequencies and to determine if there are any significant outliers from the power-law fit that may suggest the presence of QPOs. There are, however, no such outliers and we find no evidence for any QPOs in any of these three bursts.

⁴ https://github.com/danielemichilli/DM_phase

Table 1. Burst properties

Burst ID	TOA (MJD) ^a	Peak flux density (Jy) ^b	Fluence (Jy ms) ^{b,c}	Isotropic equivalent energy (10^{40} erg) ^{b,d}	Drift rate (MHz ms^{-1}) ^e	DM (pc cm^{-3})
B1	59881.86563025384	281	1089	8.1	-8(3)	219.356(12)
B2	59884.83394049601	450	474	3.5	-20(6)	219.377(9)
B3	59899.78465274653	190	411	3.1	-34(8)	219.8(1)

^a The topocentric time-of-arrival of the burst measured at the time bin of peak flux density, corrected to infinite frequency for a dispersion measure of $219.37 \text{ pc cm}^{-3}$ and using a DM constant of $1/(2.41 \times 10^{-4}) \text{ MHz}^2 \text{ pc}^{-1} \text{ cm}^3 \text{ s}$.

^b The estimated uncertainty is approximately 20% due to uncertainty in the SEFD.

^c Determined over the full bandwidth of the observations.

^d Calculated as $4\pi F \Delta\nu D_L^2 / (1+z)$, where F is the fluence, $\Delta\nu$ is the observing bandwidth, and D_L and z are the luminosity distance and redshift of the host galaxy, respectively.

^e Calculated as $\cot(\theta)$, where θ is the angle of the 2D Gaussian fit to the 2D ACF (see main text for details).

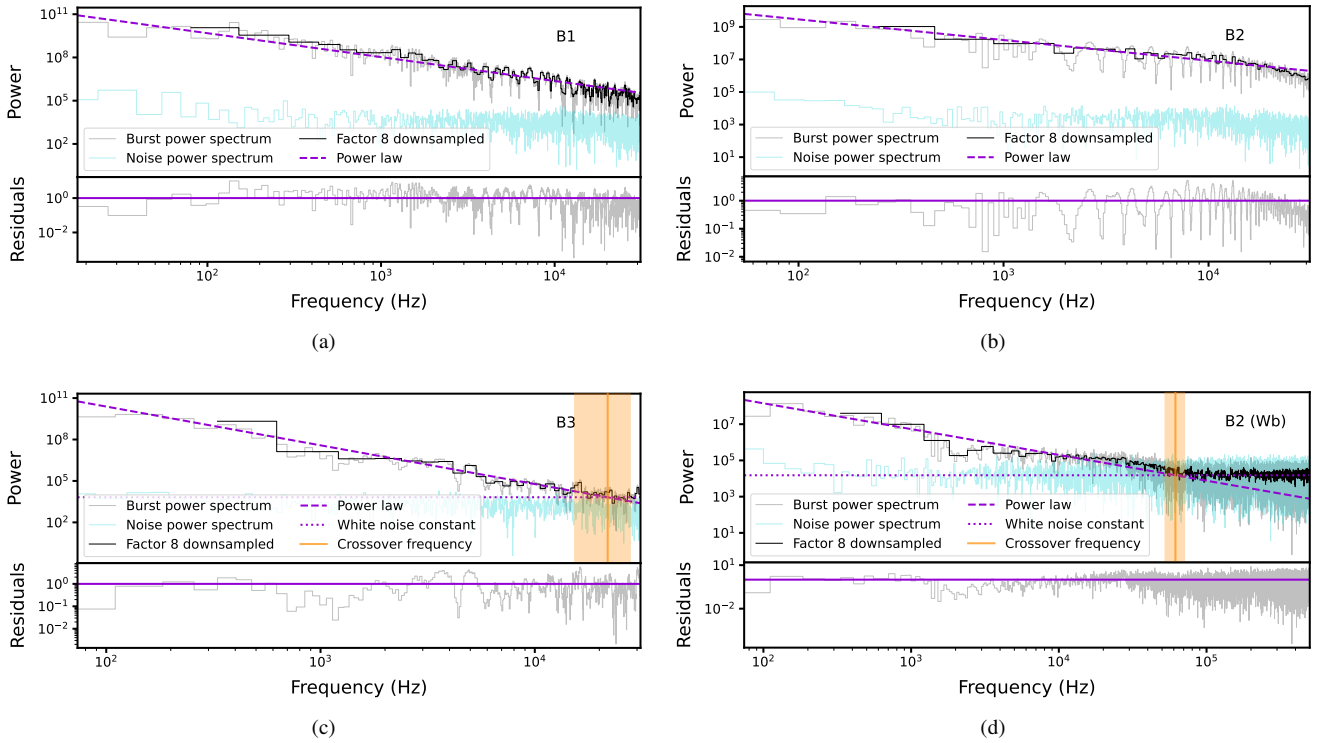


Figure 3. The power spectra of the NRT-detected bursts from FRB 20220912A are shown in grey, the black line shows the same power spectra but downsampled by a factor of 8. The power spectrum of the off-burst noise is shown in turquoise. No normalization has been applied to any of the power spectra. Burst IDs are labeled in the top right of each sub-figure. For B2, we also show the spectra using the simultaneous Westerbork (Wb) voltage data, which provided $1 \mu\text{s}$ time resolution for this analysis. The burst power spectra have been fit with a model which consists of a power-law (purple dashed line) and, where possible, a white noise component (purple dotted line) using the *Stingray* modelling interface (Huppenkothen et al. 2019). The residuals from these fits are shown in the bottom panels of each sub-figure. The crossover frequency where the power-law and white noise components intersect are marked with a solid vertical orange line, with shaded regions to illustrate the $3\text{-}\sigma$ uncertainty (see the main text for more detail). Note that the x-axes are different between bursts.

In an effort to quantify the shortest timescales present in the burst data, we determine the crossover frequency ω_c where $A\omega^\alpha$ and C intersect, i.e. the frequency where the amplitude of the source variations is smaller than the amplitude of the instrument noise and can no longer be measured. For B1 and B2, we were unable to constrain C in the NRT data, and ω_c potentially lies at frequencies higher than we are capable of probing (i.e., timescales shorter than $16 \mu\text{s}$). In addition to the power spectra and fits of the bursts in Figure 3, we also show a power spectrum of off-burst noise in turquoise. The statistical properties of the off-burst noise are different from those

of the on-burst noise due to amplitude modulation. We consequently do not normalize the spectra, and while the comparison is imperfect, it is sufficient to demonstrate that even at the highest fluctuation frequencies the burst power is well above the noise for B1 and B2. This suggests significant burst structure on timescales comparable to, and even smaller than, the time resolution of our NRT data ($16 \mu\text{s}$), which is consistent with the presence of microshots in these bursts. For B3, which lacks any obvious microshots, we were however able to constrain C and estimate ω_c to be $22(6) \text{ kHz}$ ($\sim 45 \mu\text{s}$), while for B2 with the Westerbork data ($1 \mu\text{s}$ time resolution) ω_c is $61(9) \text{ kHz}$

($\sim 16 \mu\text{s}$). These values and their uncertainties are indicated by the orange vertical lines and shaded regions in Figure 3. One can also see by eye that this is approximately the fluctuation frequency where the on- and off-burst power spectra intersect. The microshots are thus marginally resolved by the time resolution of the NRT data, and the notches present in B3 are of the same duration as some of the microshots.

3.3.3 High time resolution analysis

Using the raw voltage data recorded from the Westerbork observations, we can construct data products using SFXC (as mentioned earlier) with even better time resolution than the NRT data to confirm that we are marginally resolving the microshots and to determine if there is any structure on timescales shorter than the time resolution of the NRT data. In Figure 4 we show a dynamic spectrum of B2 which was detected using the Westerbork RT-1 dish. The plotted data have the same time resolution as the NRT data ($16 \mu\text{s}$) and a frequency resolution of 62.5 kHz. The top 3 panels show zoom-ins of the brightest three microshots at a time resolution of $1 \mu\text{s}$. Here it can be seen that the microshots are mostly being resolved in the NRT data, as they do not completely break up into more components. There are, however, hints of brightness fluctuations on the order of $1 \mu\text{s}$ timescales, particularly in the third, brightest microshot (indicated by the purple bar).

In Figure 5 we further zoom in on this specific bright microshot. Instead of plotting a conventional dynamic spectrum (with poor frequency resolution), we opt to show the time series per subband sampled at the Nyquist rate at a time resolution of 31.25 ns and a frequency resolution of 16 MHz. We find that the emission of the burst is mostly concentrated in the form of bright scintils in the top subbands. The top panel shows the time series of the microshot at a time-averaged resolution of 125 ns. Here we can see hints of sub-microsecond structure, but due to S/N limitations, the precision to which we know the true DM and the inferred scattering timescale of about $0.5 \mu\text{s}$, we are unable to make concrete claims.

3.4 Clustering of microshots

To explore whether the microshots are clustered in time during the bursts, or exhibit a random (Poisson) distribution, we manually identified 27 microshots in B1 and 18 microshots in B2, and calculated the wait-time distributions of these microshots (see Figure 6). The intervals δ between events of a Poisson process with a constant rate r follow an exponential distribution:

$$f(\delta|r) = r e^{-\delta r} \quad (2)$$

In the context of FRBs, Oppermann et al. (2018) have discussed how this can be generalized as a Weibull distribution:

$$f(\delta|k, r) = \frac{k}{\delta} (\delta r \Gamma(1+k^{-1}))^k e^{-(\delta r \Gamma(1+k^{-1}))^k} \quad (3)$$

where k is the shape parameter, r is the rate parameter, and Γ is the gamma function. If $k = 1$, the equation reduces to the exponential form and the events are Poisson distributed. The smaller the value of k , the more the distribution deviates from a Poisson distribution and the more clustered the events are.

Here we test whether the wait times between the microshots identified in these bursts are consistent with a Poissonian distribution (i.e., the posterior distribution is consistent with $k = 1$) by following the methodology of Oppermann et al. (2018) (as also implemented

in Kirsten et al. 2021; Good et al. 2023; Nimmo et al. 2023). Using a uniform prior distribution $f(k, r)$, we calculate the posterior distribution as:

$$\text{Post}(k, r|d) \propto L(d|k, r) f(k, r) \quad (4)$$

where $L(d|k, r)$ is the likelihood of the data d . The posterior probability distributions of r and k for the microshots in B1 and B2 are shown in Figure 7 and the values are presented in Table 2. For both bursts, $k < 1$, thus providing evidence that the microshots are clustered within the bursts (and possibly even to a comparable degree in both bursts).

3.5 Polarimetry

We calibrated the polarimetric data by using PSRCHIVE tools⁵ (Hotan et al. 2004). Archive files containing full polarisation information were created for the bursts using DSPSR (van Straten & Bailes 2011). These archives were then calibrated using the `pac` command from PSRCHIVE in combination with a 3-Hz pulsed noise diode scan and a polarisation calibration modeling (`pcm`) file. The `pcm` files are constructed by analyzing observations of the pulsar PSR J0742–2822 during which the receiver horn is rotated by $\sim 180^\circ$ over the course of a 1-hr observation. Notably, we do not simply apply single-axis calibration to correct the differential gain and differential phase of the receptors, but make use of the complete reception model (van Straten 2006, 2013), which in addition to the single-axis calibration, maps the frequency-dependent gain, and takes into account the non-orthogonality of the receptors to more accurately estimate the complete instrumental response (Guillemot et al., *submitted*).

To determine the RMs of the bursts, we use PSRCHIVE's `rmfit`. In Figure 8 the obtained Faraday spectra are shown for the three bursts detected with NRT. The optimal RMs, with the FWHM/SNR uncertainties reported by `rmfit`, are all close to 0 rad m^{-2} . Using IonFR (Sotomayor-Beltran et al. 2013), we estimated the amount of ionospheric Faraday rotation. All the aforementioned RM values are shown in Table 2. Importantly, the values obtained from `rmfit` are the observed RM values (RM_{obs}), since they have not been corrected for the effect of the ionosphere or redshift. These RM_{obs} values are consistent with what has been reported in other works (McKinven & Chime/Frb Collaboration 2022; Feng et al. 2023; Zhang et al. 2023). The RM also appears to be relatively stable, as Zhang et al. (2023) demonstrated that the RM changed very little over the course of 2 months. We too find no major change in the RM between B1 and B3, which are separated by 18 days.

We validated our polarimetric calibration using an observation of the pulsar PSR B0355+54. The resulting polarimetric profiles matched those in the European Pulsar Network⁶ (EPN) database centered at 1408, 1642 and 1710 MHz, and the RM we retrieved is $82.9(9) \text{ rad m}^{-2}$, which when taking into account possible ionospheric variations is consistent with $81.5(3) \text{ rad m}^{-2}$ reported in the ATNF catalogue (Manchester et al. 2005)⁷.

Figure 9 shows the polarimetric profiles of the NRT detected bursts, assuming an RM of 0.6 rad m^{-2} . Before creating the frequency-averaged profiles, we masked the frequency channels contaminated by RFI in the burst data, as well those channels that had to be masked due to RFI in the noise diode scans. Since the polarimetric

⁵ psrchive.sourceforge.net

⁶ www.epta.eu.org/epndb/

⁷ www.atnf.csiro.au/research/pulsar/psrcat/

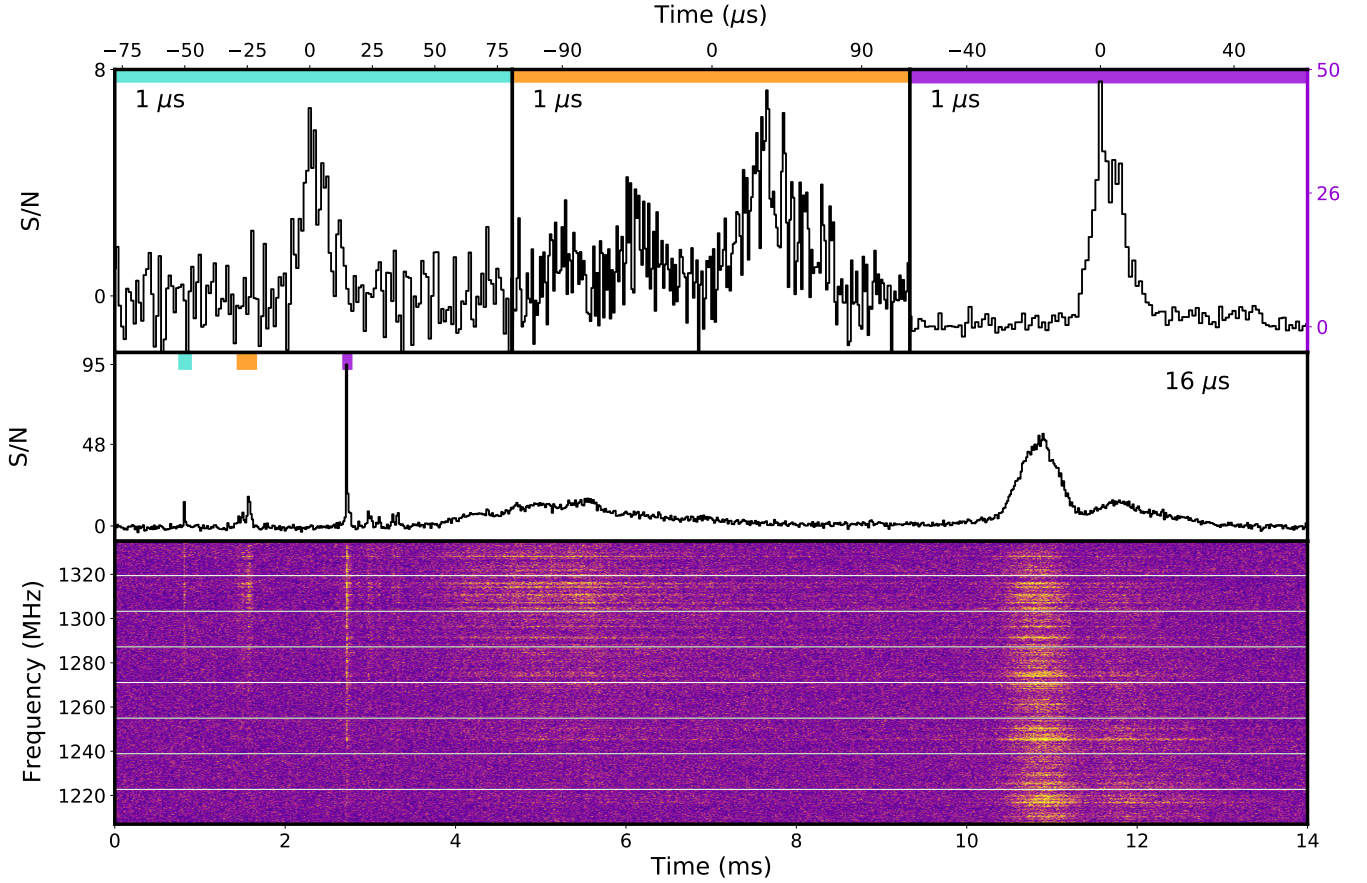


Figure 4. The bottom panel shows a zoom-in of the dynamic spectrum of burst B2, which was simultaneously detected (along with NRT) by the Westerbork RT-1 dish. The time and frequency resolution are $16 \mu\text{s}$ and 62.5 kHz , respectively, and the three brightest microshots are clearly visible. Above the dynamic spectrum, the frequency-averaged profile is shown. The top three panels show zoom-ins on each of these microshots (indicated by the coloured horizontal bars), at $1 \mu\text{s}$ time resolution. These high time resolution views of the microshots confirm that we are (mostly) resolving these microshots even with the $16\text{-}\mu\text{s}$ time resolution of the NRT data. Note that the S/N of the microshots indicated by the turquoise and orange bars is shown by the left y-axis, whereas the S/N of the microshot indicated by the purple bar is shown on the right y-axis (in purple).

Table 2. Burst properties obtained from the power spectrum, clustering, and polarimetric analyses.

Burst ID	α^a	r (ms^{-1}) ^b	k^b	RM_{obs} (rad m^{-2}) ^c	$\delta\text{RM}_{\text{obs}}$ (rad m^{-2}) ^d	Circular polarisation fraction
B1	2.08(8)	$0.87^{+1.64}_{-0.59}$	$0.46^{+0.15}_{-0.13}$	-0.93(5)	0.67(5)	4(1)
B2	1.5(2)	$1.07^{+2.40}_{-0.76}$	$0.51^{+0.22}_{-0.18}$	1.10(7)	0.73(5)	6(5)
B3	2.8(2)	-	-	0.12(7)	0.75(3)	7(2)

^a Power-law index determined by fitting a power-law model to B1-B3 using the NRT data (see the main text for more detail).

^b These uncertainties are the 99 % confidence intervals.

^c These are the FWHM/SNR uncertainties reported by `rmfit`.

^d The amount of ionospheric Faraday rotation estimated using IonFR (Sotomayor-Beltran et al. 2013).

profiles and PPAs do not significantly change if we correct for the small range of RM values that we measure, we adopt this single value which was previously reported and is consistent with our results. We used unbiased linear polarisation (Everett & Weisberg 2001) for our analyses and plots,

$$L_{\text{unbiased}} = \begin{cases} \sigma_I \sqrt{\left(\frac{L}{\sigma_I}\right)^2 - 1} & \text{if } \frac{L}{\sigma_I} \geq 1.57 \\ 0 & \text{otherwise} \end{cases} \quad (5)$$

The bursts are all about 100% linearly polarised with hints of

circular polarisation in some components. The circular polarisation fractions are tabulated in Table 2. We do not believe these inklings of circular polarisation to be astrophysical, since the circular polarisation fraction of the bursts still retains a slight frequency dependence despite our careful calibration procedure (see Figure C1). Nevertheless, this imperfection in the calibration has no significant effects on our results or interpretation thereof. Unlike many other repeating FRBs which show PPAs that are flat across, and even between, bursts (e.g., Nimmo et al. 2021), the PPAs of these FRB 20220912A bursts

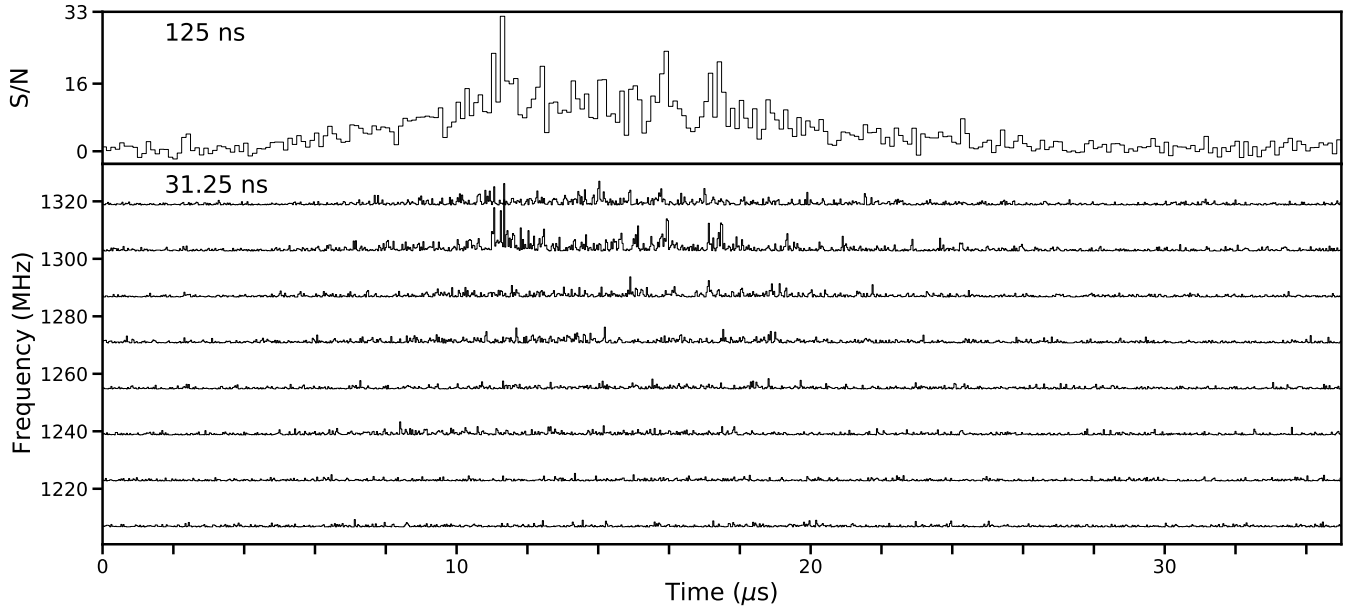


Figure 5. The top panel shows the brightest microshot in burst B2 at 125 ns time resolution. In the bottom panel the time profile for each of the eight subbands is shown at a time resolution of 31.25 ns, which is the best possible time resolution we can obtain with the Westerbork data. The majority of the emission is concentrated towards the top of the Westerbork observing band.

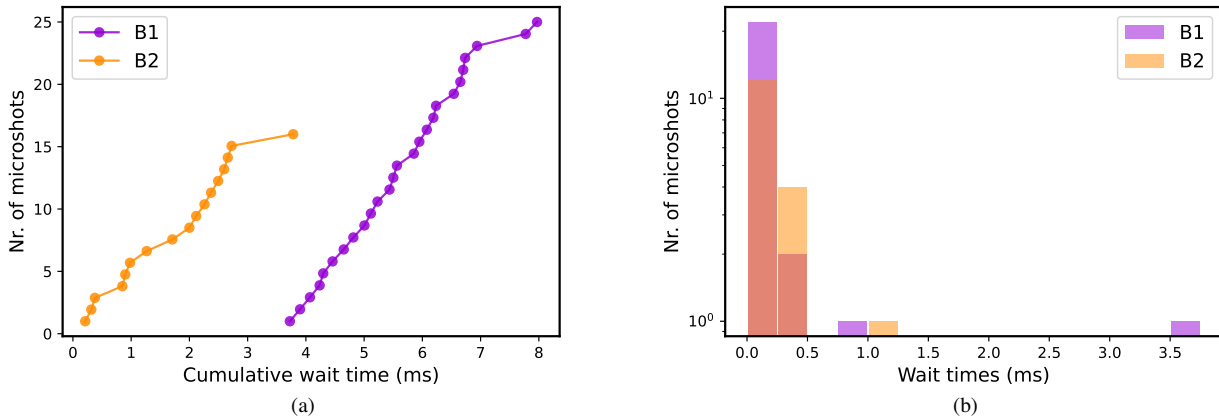


Figure 6. (a) The cumulative microshot distribution as a function of time since the start of the burst, for bursts B1 and B2. (b) The wait-time distribution of the microshots identified in B1 and B2. Each histogram bin is 0.25 ms wide.

show some variability. The PPAs in B1 and B3 display swings and vary by approximately 10 degrees across the burst duration. We also see significant jumps in the PPA at the time of the dense microshot forest. Feng et al. (2023) also reported PPA swings in some bursts from FRB 20220912A, akin to those seen in FRB 20180301 (Luo et al. 2020).

4 DISCUSSION

4.1 On dedispersion

The DM is a fundamental quantity associated with FRB sources, and knowledge of the correct DM is critical for measuring many other attributes such as burst widths, peak flux densities and scattering

timescales, to only name a few examples. Determining the DM accurately, however, is non-trivial as has been noted by various other authors (e.g., Hessels et al. 2019).

One can opt to determine the DM by trying to maximise the frequency-averaged S/N of a burst, as is effectively done in most burst searches. This method unfortunately often results in overestimation of the DM due to downward drifting complex frequency-time structure (‘sad-tromboning’; Hessels et al. 2019) which is present in many FRBs (especially repeaters) and is most likely not related to dispersion caused by intervening media. Hessels et al. (2019) followed an alternate approach which involves trying to optimise for burst structure by maximizing the time derivative of the peaks in frequency-averaged burst profile. This method has been widely adopted through its implementation in the `DM_phase` package (Seymour et al. 2019) and other similar techniques. While this greatly

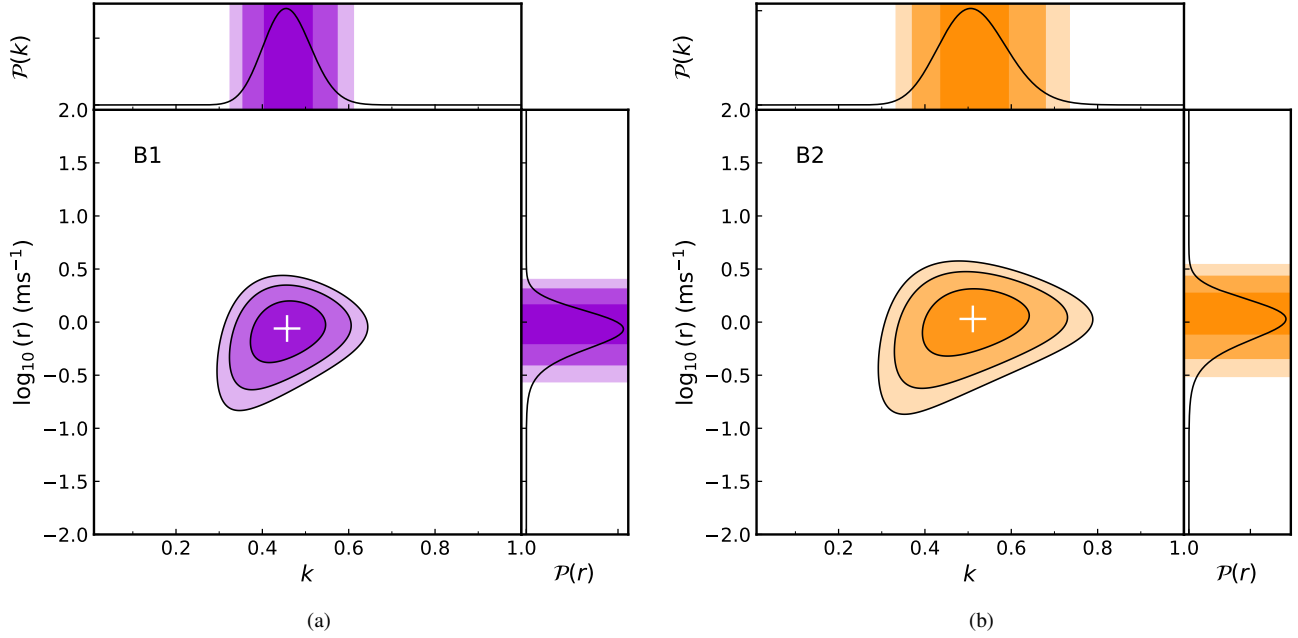


Figure 7. Posterior probability distributions of the rate (r) and shape parameters (k) for the Weibull distributions of the microshots identified in B1 (a) and B2 (b). The contours and shaded regions show the 68%, 95% and 99% confidence intervals. The white plus indicates the position of the maximum probability density.

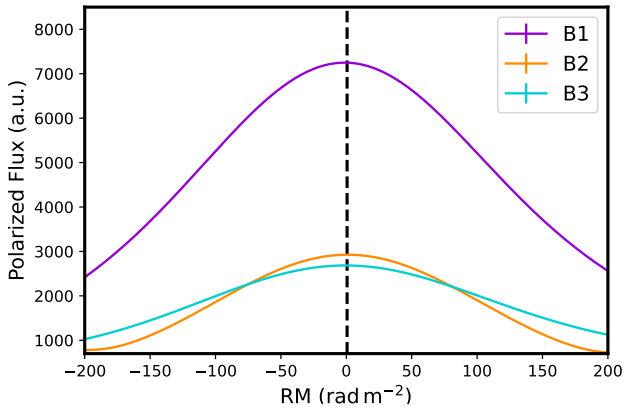


Figure 8. The RM spectra produced by `rmfit` for the three FRB 20220912A bursts detected with the NRT. The optimal values for RM_{obs} are $-0.93(5)$, $1.10(7)$ and $0.12(7)$ rad m^{-2} for B1, B2 and B3, respectively. The vertical dashed line is at 0.6 rad m^{-2} , the RM reported for a bright burst from FRB 20220912A by CHIME/FRB (McKinven & Chime/Frb Collaboration 2022).

improves upon simple S/N-maximization, it might still fail to determine an accurate DM for weaker bursts or bursts which lack any prominent structure.

Fortunately, bursts B1 and B2 exhibit exquisite structure. There are exceptionally bright components present that are at most only a few bins wide in the NRT data (tens of microseconds in duration). As was mentioned in Section 3, we determined the DM of the bursts presented in this paper by aligning the microshots so that the emission occurs simultaneously at all frequencies. The DM estimates obtained from using `DM_phase`, with some manual guidance on what range of

times and fluctuation frequencies to use, are consistent with our DM values.

Importantly, in accurately determining this DM a few assumptions are made that require justification. Firstly, we are assuming that the entire burst, and all of its components, have a single DM value. Furthermore, the structure optimization approach assumes that in the reference frame of the source, burst emission occurs simultaneously across a broad range of frequencies. Building upon these two assumptions, we further assume that it only holds true for the microshots, but not necessarily for broader components/sub-bursts. This is motivated by our observation of a residual drift that can be seen in the broader sub-bursts after correcting for dispersion (using a DM which we measure using the microshots). While, effectively, a single DM value temporally aligns the emission of multiple microshots across all observed frequencies, it does not vertically straighten the broader components in the dynamic spectrum. We have overdedispersed bursts B1 and B2 to straighten these broader burst components, ignoring the microshots, and find that no single DM value can perfectly straighten all of the broader burst components, as they have slightly different (apparent) DMs. These DMs are always slightly larger than the DM determined using the microshots, but smaller than about 0.3 pc cm^{-3} . Other authors have also noted that for some bursts not all components can be temporally aligned using a single DM (e.g., Michilli et al. 2018; Zhou et al. 2022). In addition to the λ^2 dependent delay introduced by dispersion, there appears to be an additional drift which determines the spectro-temporal morphology of the sub-bursts, perhaps related to the emission mechanism. Jahns et al. (2023) and Chamma et al. (2021) have noted that this drift increases linearly with burst duration, and that the sad-trombone effect occurs within sub-bursts, as well as between them.

Alternatively, if we refrain from making our initial assumption and allow for different burst components to have different DM values, the residual drift seen in broader burst components after dedispersion (to the microshot-determined DM) could perhaps be explained by

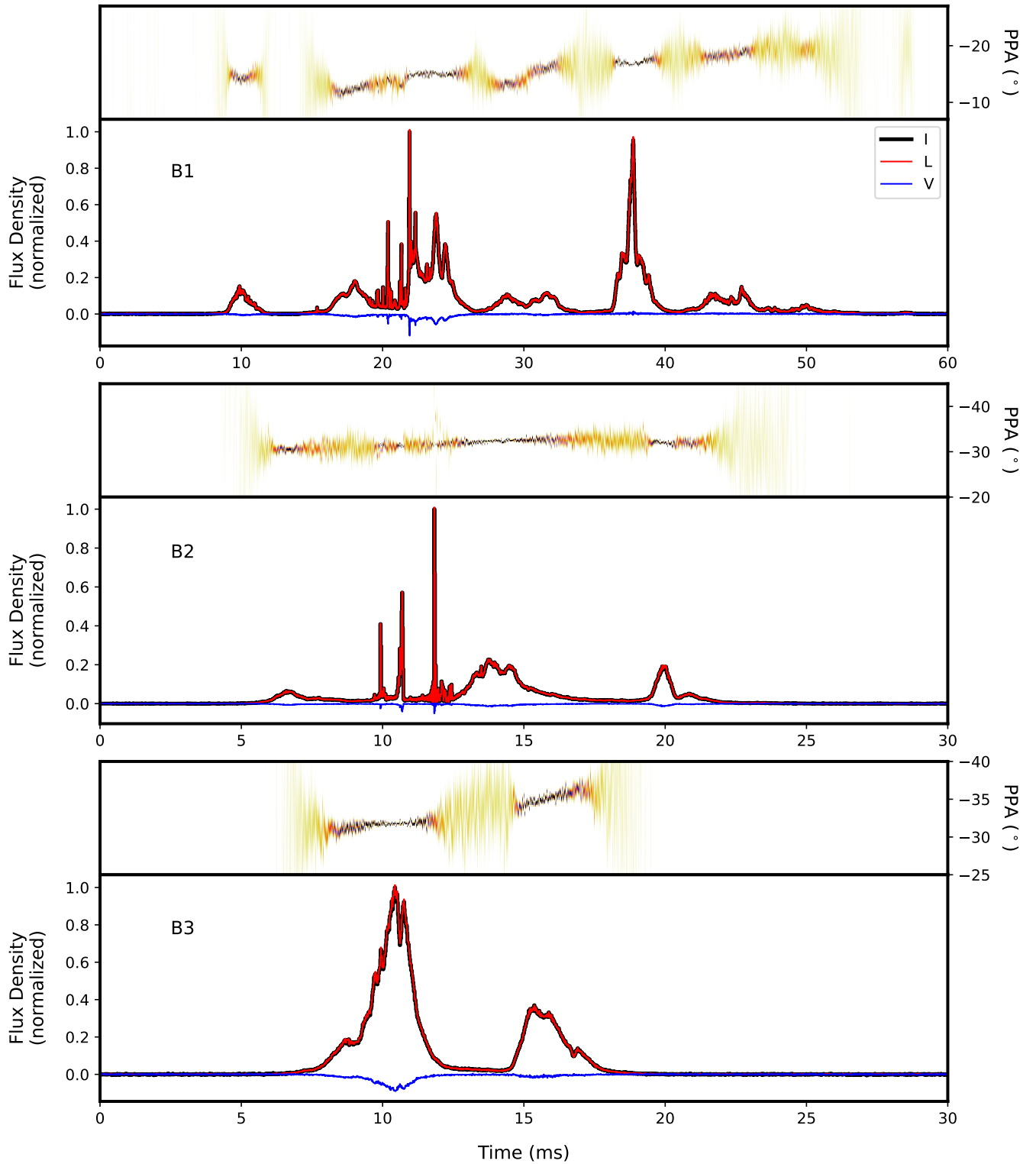


Figure 9. Polarimetric profiles of the three FRB 20220912A bursts detected with the NRT (see burst ID in each sub-figure). The total intensity is shown by the black burst profiles and the unbiased linear and circular polarisation in red and blue, respectively. These profiles are shown at the full $16\text{-}\mu\text{s}$ time resolution of the data, and channels contaminated by RFI were flagged before averaging over frequency to obtain these profiles. The probability distribution (following [Everett & Weisberg 2001](#)) of the PPAs are shown in the panels above the burst profiles, and are zoomed-in to show subtle variations with time. These profiles have been polarimetrically calibrated using the full receptor model and de-Faradayed with an RM of 0.6 rad m^{-2} .

a difference in column depth or electron density between the microshots and the broader burst components. Considering a scenario where FRBs are emitted within an ionised medium around a compact progenitor, the difference in DM would arise from the broader components being emitted deeper within the ionised medium closer to the progenitor, and thus travelling along a longer path or through denser media than the microshots. Furthermore, within close proximity to a magnetar progenitor, for example, the plasma becomes relativistic and nonlinear propagation effects start to play a significant role. The most important nonlinear propagation effect in magnetar winds is the filamentation instability (Sobacchi et al. 2022), which is expected to result in slight variations of the effective DM, on the order of the variations we see in different millisecond-duration components in these bursts.

Now, considering a scenario where the position of the burst emission can be explained by radius-to-frequency mapping (Lyutikov 2020; Tong et al. 2022), it is more natural to assume that the burst emission of some components is delayed at lower frequencies as a result of material that is propagating radially outward from a central engine, than assuming the inverse situation where emission is delayed at higher frequencies due to the emission region moving towards the central engine. Consequently, if a burst is found to have a DM that results in dedispersed emission occurring later at higher frequencies, this DM is likely overestimated.

In short, we thus argue that the correct DM of a burst, is one that temporally aligns short timescale emission at all observed frequencies, but may still cause longer duration sub-bursts to have a drift where emission is delayed at lower, but not higher, frequencies. The shortest timescales in a burst should thus be used to quantify the uncertainty of the DM measurement. Methods that enable accurate quantification of the uncertainty on the structure metric of a burst, such as Sutinjo et al. (2023), are especially useful in this regard.

Reporting accurate uncertainties is especially important when individual DM measurements are made for a large numbers of bursts. Negligence in this regard may result in nonphysical interpretations, as significant changes in the DM of bursts within a short period of time requires quite extreme variations in the line-of-sight plasma local to the source (e.g., very dense filaments moving across the line-of-sight). In the case of the Crab pulsar, DM variations of $\sim 0.02 \text{ pc cm}^{-3} \text{ month}^{-1}$ have been seen that can be interpreted as a scattering screen caused by filaments in the nebula (Driessen et al. 2019). While some FRBs do originate from a very extreme magneto-ionic environment, and large DM and RM variations between bursts are expected, true astrophysical DM variations of a few units over the course of a few weeks seem unlikely. We therefore argue that it is in general better and more astrophysically motivated (although still not ideal) to dedisperse multiple bursts that were detected from the same source within a period of weeks, to a DM which has been determined from burst(s) that have short timescale structures, than it to dedisperse each burst to an individual DM (regardless of the method used to determine these individual DMs).

Notably, however, there are some sources, such as FRB 20121102A have been seen to have credible DM variations on longer timescales. The DM has been seen to increase by approximately 4 pc cm^{-3} over the course of ~ 3 years (Michilli et al. 2018; Hilmarsson et al. 2021), before decreasing by about 10 pc cm^{-3} over the next 3 years (Wang et al. 2022).

4.2 Microshots in FRB 20220912A

Two of the three FRB 20220912A bursts presented in this paper consist of burst components with durations ranging from about ten

microseconds to a few milliseconds. Summing over the entire 512-MHz observing bandwidth, the brightest of these microshots in B2 (when dedispersed using a DM of $219.377 \text{ pc cm}^{-3}$) has a S/N above 2000, corresponding to a peak flux density of approximately 450 Jy. These microshots appear to be mostly resolved at around $10 \mu\text{s}$, but there are hints of sub-microsecond time structure, as shown in Figure 5, that require confirmation.

In addition to the microshots there are also more typical wider burst components. Interestingly, even after the burst has been corrected for dispersion and the microshots are aligned so that emission occurs simultaneously at all frequencies, the wider burst components still exhibit a residual drift apparently not associated with dispersion (see, e.g., the components between 5 and 6 ms in B1 of Figure 2). Assuming the microshots with comparable bandwidth are also drifting, on a conservative estimate of 5 time bins, this results in a drift rate which is at least a factor of 6 larger than the more typical sub-bursts.

The range of timescales we are probing is also evident in the NRT burst power spectra, where there is power significantly above the noise level for frequencies ranging from $\sim 40 - 3 \times 10^4 \text{ Hz}$ (corresponding to timescales of $\sim 32 \mu\text{s} - 25 \text{ ms}$) for B1 and B2. For B3, which lacks the microshots, the crossover frequency starts becoming visible and suggests the shortest timescales on which there is significant burst structure is about $35 - 62 \mu\text{s}$, above the duration of the shortest microshots but corresponding to the duration of the notches. The Westerbork B2 power spectrum indicates that the shortest timescale where there is significant structure is around $14 - 19 \mu\text{s}$, explaining why the crossover frequency could not be determined in the NRT data, but that the shots are being marginally resolved.

Furthermore, we have shown in Section 3.4 that these microshots are not homogeneously spread out through the burst, but are clustered into dense forests that can be described by a Weibull shape parameter of about 0.5. The different timescales of burst emission and different drift rates, together with the clustering of the microshots, require theoretical understanding

4.3 In comparison with FRBs

It is well known that temporal structure much shorter than the burst width can be present in FRBs. Farah et al. (2018) showed that FRB 170827 has structures that are only $\sim 30 \mu\text{s}$ in duration, and the total duration of one of the FRB 20121102A bursts in Michilli et al. (2018) is only $\sim 30 \mu\text{s}$. FRB 20180916B bursts can have structure on the order of a few microseconds (Nimmo et al. 2021), and even shorter timescale structure (tens of nanoseconds) is present in some FRB 20200120E bursts (Nimmo et al. 2022). Additionally, in a search of archival GBT data, Snelders et al. (2023) detected isolated bursts from FRB 20121102A that are only a few microseconds in duration. At least some repeaters are thus capable of producing such short timescale emission independent from broad-timescale emission. We have shown that the FRB 20220912A bursts presented in this work have structure on timescales down to a few microseconds, and potentially even lower (see Figure 5), adding FRB 20220912A to the handful of FRBs that exhibit known microstructure.

However, we do not see these forests of microshots in all bursts from FRB 20220912A. Similarly, Nimmo et al. (2021, 2022, 2023) noted that only some of the bursts have microstructure. This raises the question if these microshots are in fact a type of burst which can sometimes occur alone as with FRB 20121102A or FRB 170827, and at other times simultaneously with a different broader type of burst, as with B1 and B2 presented here. While the isolated microsecond duration FRBs might be ‘tips of an iceberg’ — extraordinarily bright microshots (much brighter than the ones shown in this work) from a

broader burst too faint to be detected — this seems unlikely because of the fine-tuning that is needed to see microshots but no broader components (Snelders et al. 2023). Regardless, investigating emission on a wide range of timescales provides valuable constraints for theoretical models.

The occurrence of microshots is not easily explained by propagation effects such as fragmentation instabilities (e.g., Lu et al. 2022). One of the main arguments for this is the lack of explanation as to why the instability would cause the breakdown of the emission into the microshots, while not affecting the broader emission components that occur mere milliseconds later. Ignoring relativistic effects, these timescales correspond to small emission regions which are more naturally explained by magnetospheric magnetar models (Beniamini & Kumar 2020) than the synchrotron maser models where emissions are generated in a shock far away from the central engine (e.g., Metzger et al. 2019).

4.4 In comparison with neutron stars

There are five known Galactic radio-emitting magnetars (Camilo et al. 2006, 2007; Levin et al. 2010; Eatough et al. 2013; Karuppusamy et al. 2010). These magnetars emit radio pulsations that while semi-stable in rotational phase, show pulse-to-pulse variability in flux density, spectral index and the shape of the pulse profile (e.g., Lazaridis et al. 2008; Serylak et al. 2009). Similarly to the bursts seen from repeating FRBs, the individual magnetar radio pulses (as well as the average pulse profile) tend to be highly linearly polarised, while having circular polarisation up to a few tens of percent (e.g., Kramer et al. 2007), although this too can be time variable (Dai et al. 2019). Furthermore, individual radio pulses from magnetars have often been described as ‘spiky’ in the literature (e.g., Serylak et al. 2009; Caleb et al. 2022). The pulses jump around in phase within the larger integrated profile, and are typically a few milliseconds wide, and sometimes exceptionally bright (e.g., Yan et al. 2015; Pearlman et al. 2018; Suresh et al. 2021). The pulses can also occasionally show hints of more complex structure, such as features as short as ≈ 0.2 ms (Camilo et al. 2006) or two components with opposing spectral indices (Suresh et al. 2021), further prompting comparison with FRBs. While the radio pulsations are the defining characteristic of radio magnetars, these pulsations are not necessarily ever-present and can disappear as in the case of XTE J1810–197 (Camilo et al. 2016), or reawaken after years of radio-quiescence (Lyne et al. 2018). We require long-term monitoring of more repeaters to determine whether the burst storm behaviour is analogous to this. Unlike FRBs that are sometimes extremely narrowband (~ 10 – 30% fractional bandwidths, e.g., Gourdjji et al. 2019; Kumar et al. 2021), the magnetar pulsations have broadband flat spectra (e.g., Lazaridis et al. 2008; Dai et al. 2019). The pulses also do not show any downward drifting or sad-tromboning, as is evident in some bursts from repeaters. Magnetar radio bursts have not been extensively studied on microsecond timescales, however, and the comparison with FRBs is thus incomplete.

It is also worth noting that even the shortest timescale components in typical magnetar pulses are still longer in duration than the microshots in the FRB 20220912A bursts presented here, or the microshots seen in giant pulses (GPs). GPs are extremely bright pulses from pulsars that last a few microseconds or less, and that occur within narrow phase windows. GPs have also been detected from radio magnetars (e.g., Caleb et al. 2022). GPs from the Crab (PSR B0531+21) have been shown to occasionally consist of nanosecond-duration highly polarised shots of emission (Hankins et al. 2003). The main pulse (MP) of the Crab has also been

shown to resolve down to a dense forest of broadband microsecond bursts, which sometimes can be further resolved into extremely bright ($> 10^3$ Jy), highly polarised and narrow-band nano-shots with sub-nanosecond durations (Hankins & Eilek 2007). While morphologically similar to the spiky emission in magnetars and the microshots in FRBs, it is important to note that the timescales are much shorter for the GPs. Furthermore, the polarimetric properties of the nanoshots in the MP can change drastically from one shot to another, meaning that with sufficient averaging or a high enough density of nanoshots, the polarization washes out and the profile becomes only weakly polarized. As pointed out by other authors, pulses from the High-Frequency Interpulse (HFIP) share more similarity with the repeaters in that they are often highly linearly polarised (~ 80 – 100%), have little to no circular polarisation and have polarisation positions angles that remain constant not only throughout the pulse, but also between pulses (Hankins et al. 2016). This thus proves to show that magnetised neutron stars such as the Crab are capable of producing burst emission with very diverse properties.

The only Galactic radio burst brighter than GPs, are the extremely bright isolated radio bursts that have been detected from the Galactic magnetar SGR 1935+2154 (Bochenek et al. 2020; CHIME/FRB Collaboration et al. 2020). The brightest of these bursts had an equivalent isotropic energy approximately a thousand times brighter than any previously detected radio magnetar burst; this burst was indeed even more luminous than bursts detected from the extragalactic FRB 20200120E (Nimmo et al. 2022) situated approximately 3.6 Mpc away (Bhardwaj et al. 2021; Kirsten et al. 2022a). It was further shown in follow-up observations that SGR 1935+2154 is also capable of producing fainter bursts, spanning 7 orders of magnitude in energies with comparable rates (Kirsten et al. 2021). All together, this shows that at least some fraction of the FRB population is produced by magnetars. Assuming a magnetar progenitor, the discovery of an FRB source in a globular cluster (Kirsten et al. 2022a), does however beckon for formation channels other than core-collapse supernovae, such as accretion-induced collapse or binary merger.

4.5 In comparison with solar radio bursts

The Sun produces various types of solar radio bursts (SRBs) that bear striking morphological similarities with FRBs, albeit on much longer timescales and with much lower luminosity (for a review see, e.g., Wild et al. 1963; Pick & Vilmer 2008). In fact, Lyutikov (2002) predicted coherent radio emission similar to SRBs during X-ray bursts from soft gamma-ray repeaters, by virtue of comparison with solar flares. The first three types of SRBs were coined by Wild & McCready (1950). Type I SRBs (also called ‘noise storms’) can last from hours to days, with the emission typically observed between 50 – 500 MHz and are made up of short-duration (~ 1 s) and narrow bandwidth bursts which occur on top of continuum emission. Type II and Type III SRBs have more complex structure and exhibit time-frequency drifting on the order of ~ 0.25 and ~ 20 MHz s^{-1} , respectively. Type II SRBs last approximately minutes and are associated with coronal mass ejections that create a shock that propagates outward through the solar corona, while Type III SRBs last only tens of seconds and are associated with high-velocity electrons that are accelerated along open magnetic field lines resulting from magnetic reconnection events that cause solar flares. Ignoring the duration of the emission, the downward drifting structure of Type II and III bursts looks very similar to repeater FRB emission, and also specifically to the broader emission components and microshots seen in the FRB 20220912A bursts presented here. However, it is worth noting that SRBs can be significantly circularly polarized (e.g., Kansabanik

2022), whereas repeaters are more typically highly linearly polarized. This could potentially be attributed to the emission being relativistic in the latter case. There are also other types of SRBs and more elaborate sub-classifications, but discussion thereof is not required for the comparison being made in this work.

The different types of SRBs are produced by different emission mechanisms, and while the emission physics are naturally vastly different from that of FRBs which are many order of magnitudes more energetic and shorter in duration, this provides an interesting analogy for the FRB 20220912A bursts presented in this paper. Just as the Sun produces different types of bursts through different processes, sometimes simultaneously, FRB sources could potentially be generating different types of bursts (in terms of energy, duration, bandwidth or drift rate), that are occasionally superimposed. In the solar scenario the outward propagating shock of a coronal mass ejection results in longer duration, lower drift rate Type II bursts, but around the same time short-duration, higher-drift-rate Type III bursts can be produced along the open field lines. One of the models that has been proposed to explain magnetar X-ray bursts, and that has been adapted to also explain FRBs, is the magnetar fireball model. In this model energy arising from starquakes or magnetic reconnection is injected into a plasmoid which is enclosed by magnetic field lines close to the surface of the magnetar. As the fireball expands along the magnetic field lines, the energy can dissipate as coherent radio emission resulting in FRBs (Ioka 2020; Wada & Ioka 2023). The observed spectrum of the emission is dependent on the configuration of the magnetic field. In analogy to the SRBs, the microshots and broader drifting components we observe in these FRB 20220912A bursts could potentially be emission with different drift rates arising from different magnetic field configurations.

5 CONCLUSIONS & FUTURE WORK

We have observed the highly active repeating FRB 20220912A using the Nançay and Westerbork radio telescopes. We analyze a small subset of bursts with extremely high S/N, dynamic range, and time resolution. These data allow us to investigate effects that may likely be present in the bursts from other FRBs, but unapparent due to their faintness or lack of time resolution used in the data recording. We come to the following main conclusions and suggestions for future work:

- As previously pointed out by other authors (Hessels et al. 2019), the determination of FRB DMs is non-trivial because of frequency-dependent burst structure and time-frequency drifts that are unlikely to be related to dispersion in the intervening media. Here we have used broadband microshots in FRB 20220912A bursts to determine the optimal DM. We find that while the microshots are well fit by a single DM, there is a residual drift in the broader burst components. This means that DM determination via frequency-averaged burst structure maximization will likely fail for bursts with lower S/N. We thus caution that DM variation in repeating FRBs is difficult to establish robustly, and that DM uncertainties should consider the shortest-observable time structures (Sutinjo et al. 2023).

- After accurate correction for dispersion, we still observe residual time-frequency drifts within broader sub-bursts of FRB 20220912A. This residual time-frequency drift may be related to an outwards propagating emission region and radius-to-frequency mapping (Hessels et al. 2019). Alternatively, it could be due to an additional electron column density between the emission sites of the broad and narrow (microshots) burst components; the DM required to straighten the broad burst components is $\lesssim 0.3 \text{ pc cm}^{-3}$.

- We show that some FRB 20220912A bursts have brightness variations spanning from a few milliseconds to less than a microsecond. Such a broad range of timescales, within a single burst event, has also been observed in FRB 20180916B (Nimmo et al. 2021) and FRB 20200120E (Nimmo et al. 2022). Furthermore, we find that the brightest microshots in our observed bursts are clustered in time compared to the total duration of the bursts. The range of timescales and clustering of microshots requires theoretical understanding. Since the microshots show extremely high (or possibly no) time-frequency drift, it is possible that they arise from a distinct physical mechanism compared to the broader sub-bursts, which do drift.

- Though solar radio bursts (SRBs) are obviously very different in their luminosity and timescale, the existence of multiple types of SRBs, which sometimes occur superimposed on each other provides an interesting analogy to consider. The broadband microshots from FRB 20220912A could be generated in a physically distinct way compared to the wider frequency-swept emission. Supporting this hypothesis, Snelders et al. (2023) find isolated microshots from FRB 20121102A, which occur at different times compared to wider, time-frequency swept bursts. However, the similar polarimetric properties between the microshots and wider sub-bursts suggests a physical connection.

- The timescales of the FRB 20220912A microshots are compatible with those of giant pulses from young and millisecond rotation-powered pulsars (e.g., Hankins et al. 2016), but the overall FRB 20220912A burst durations of tens of milliseconds are much longer. While the overall durations and spiky burst structure are consistent with pulses from radio magnetars, sub-millisecond temporal structures have not been extensively studied in magnetars. We therefore encourage microsecond-resolution studies of bright radio bursts from magnetars.

ACKNOWLEDGEMENTS

DMH would like to thank Pawan Kumar and Emanuele Sobacchi for helpful discussions about the interpretation of the results presented in this work. Research by the AstroFlash group at University of Amsterdam, ASTRON and JIVE is supported in part by an NWO Vici grant (PI Hessels; VI.C.192.045). The Nançay Radio Observatory is operated by the Paris Observatory, associated with the French Centre National de la Recherche Scientifique (CNRS). We acknowledge financial support from the “Programme National de Cosmologie et Galaxies” (PNCG) and “Programme National Hautes Energies” (PNHE) of CNRS/INSU, France. The Westerbork RT-1 telescope is maintained and operated by ASTRON. We express our gratitude to the operators R. Blaauw, J.J. Sluman and H. Mulder for scheduling observations. We would like to express our gratitude to Aard Keipema and Willem van Straten for modifying the software correlator SFXC, and software package DSPSR, respectively, to fit our needs. DH is supported by the Women In Science Excel (WISE) programme of the Netherlands Organisation for Scientific Research (NWO).

DATA AVAILABILITY

The relevant code and data products for this work will be uploaded on Zenodo at the time of acceptance for publication.

REFERENCES

- Aggarwal K., Law C. J., Burke-Spolaor S., Bower G., Butler B. J., Demorest P., Linford J., Lazio T. J. W., 2020a, *Research Notes of the American Astronomical Society*, 4, 94
- Aggarwal K., et al., 2020b, *Journal of Open Source Software*, 5, 2750
- Beniamini P., Kumar P., 2020, *MNRAS*, 498, 651
- Bhandari S., et al., 2022, *AJ*, 163, 69
- Bhardwaj M., et al., 2021, *ApJ*, 910, L18
- Bhusare Y., et al., 2022, *The Astronomer's Telegram*, 15806, 1
- Bochenek C. D., Ravi V., Belov K. V., Hallinan G., Kocz J., Kulkarni S. R., McKenna D. L., 2020, *Nature*, 587, 59
- CHIME/FRB Collaboration et al., 2020, *Nature*, 587, 54
- Caleb M., et al., 2022, *MNRAS*, 510, 1996
- Camilo F., Ransom S. M., Halpern J. P., Reynolds J., Helfand D. J., Zimmerman N., Sarkissian J., 2006, *Nature*, 442, 892
- Camilo F., Ransom S. M., Halpern J. P., Reynolds J., 2007, *ApJ*, 666, L93
- Camilo F., et al., 2016, *ApJ*, 820, 110
- Chamma M. A., Rajabi F., Wyenberg C. M., Mathews A., Houde M., 2021, *MNRAS*, 507, 246
- Chatterjee S., et al., 2017, *Nature*, 541, 58
- Chime/Frb Collaboration et al., 2020, *Nature*, 582, 351
- Chime/Frb Collaboration et al., 2023, *ApJ*, 947, 83
- Chime/Frb Collaboration 2021, *The Astronomer's Telegram*, 14497, 1
- Connor L., Miller M. C., Gardenier D. W., 2020, *MNRAS*, 497, 3076
- Cordes J. M., Lazio T. J. W., 2002, *arXiv e-prints*, pp astro-ph/0207156
- Cruces M., et al., 2021, *MNRAS*, 500, 448
- Dai S., et al., 2019, *ApJ*, 874, L14
- Day C. K., et al., 2020, *MNRAS*, 497, 3335
- Desvignes G., Barott W. C., Cognard I., Lespagnol P., Theureau G., 2011, in Burgay M., D'Amico N., Esposito P., Pellizzoni A., Possenti A., eds, *American Institute of Physics Conference Series Vol. 1357, Radio Pulsars: An Astrophysical Key to Unlock the Secrets of the Universe*. pp 349–350, doi:10.1063/1.3615154
- Driessen L. N., Janssen G. H., Bassa C. G., Stappers B. W., Stinebring D. R., 2019, *MNRAS*, 483, 1224
- Eatough R. P., et al., 2013, *Nature*, 501, 391
- Everett J. E., Weisberg J. M., 2001, *ApJ*, 553, 341
- Farah W., et al., 2018, *MNRAS*, 478, 1209
- Feng Y., et al., 2022, *The Astronomer's Telegram*, 15723, 1
- Feng Y., et al., 2023, *arXiv e-prints*, p. arXiv:2304.14671
- Gajjar V., et al., 2018, *ApJ*, 863, 2
- Good D. C., et al., 2023, *ApJ*, 944, 70
- Gopinath A., et al., 2023, *arXiv e-prints*, p. arXiv:2305.06393
- Gordon A. C., et al., 2023, *arXiv e-prints*, p. arXiv:2302.05465
- Gourdji K., Michilli D., Spitler L. G., Hessels J. W. T., Seymour A., Cordes J. M., Chatterjee S., 2019, *ApJ*, 877, L19
- Hankins T. H., Eilek J. A., 2007, *ApJ*, 670, 693
- Hankins T. H., Kern J. S., Weatherall J. C., Eilek J. A., 2003, *Nature*, 422, 141
- Hankins T. H., Eilek J. A., Jones G., 2016, *ApJ*, 833, 47
- Hessels J. W. T., et al., 2019, *ApJ*, 876, L23
- Hewitt D. M., et al., 2022, *MNRAS*, 515, 3577
- Hilmarsson G. H., et al., 2021, *ApJ*, 908, L10
- Hotan A. W., van Straten W., Manchester R. N., 2004, *Publ. Astron. Soc. Australia*, 21, 302
- Huppenkothen D., et al., 2019, *ApJ*, 881, 39
- Ioka K., 2020, *ApJ*, 904, L15
- Jahns J. N., et al., 2023, *MNRAS*, 519, 666
- Kansabanik D., 2022, *Sol. Phys.*, 297, 122
- Karuppusamy R., Stappers B. W., van Straten W., 2010, *A&A*, 515, A36
- Keimpema A., et al., 2015, *Experimental Astronomy*, 39, 259
- Kirsten F., Snelders M. P., Jenkins M., Nimmo K., van den Eijnden J., Hessels J. W. T., Gawroński M. P., Yang J., 2021, *Nature Astronomy*, 5, 414
- Kirsten F., et al., 2022a, *Nature*, 602, 585
- Kirsten F., et al., 2022b, *The Astronomer's Telegram*, 15727, 1
- Kramer M., Stappers B. W., Jessner A., Lyne A. G., Jordan C. A., 2007, *MNRAS*, 377, 107
- Kumar P., et al., 2021, *MNRAS*, 500, 2525
- Lazaridis K., Jessner A., Kramer M., Stappers B. W., Lyne A. G., Jordan C. A., Serylak M., Zensus J. A., 2008, *MNRAS*, 390, 839
- Levin L., et al., 2010, *ApJ*, 721, L33
- Li D., et al., 2021, *Nature*, 598, 267
- Lu W., Beniamini P., Kumar P., 2022, *MNRAS*, 510, 1867
- Luo R., et al., 2020, *Nature*, 586, 693
- Lyne A., Levin L., Stappers B., Mickaliger M., Desvignes G., Kramer M., 2018, *The Astronomer's Telegram*, 12284, 1
- Lyutikov M., 2002, *ApJ*, 580, L65
- Lyutikov M., 2020, *ApJ*, 889, 135
- Manchester R. N., Hobbs G. B., Teoh A., Hobbs M., 2005, *AJ*, 129, 1993
- Marcote B., et al., 2017, *ApJ*, 834, L8
- Marcote B., et al., 2020, *Nature*, 577, 190
- Margalit B., Beniamini P., Sridhar N., Metzger B. D., 2020, *ApJ*, 899, L27
- McKinven R., Chime/Frb Collaboration 2022, *The Astronomer's Telegram*, 15679, 1
- Mckinven R., et al., 2023, *ApJ*, 951, 82
- Metzger B. D., Margalit B., Sironi L., 2019, *MNRAS*, 485, 4091
- Michilli D., et al., 2018, *Nature*, 553, 182
- Nimmo K., et al., 2021, *Nature Astronomy*, 5, 594
- Nimmo K., et al., 2022, *Nature Astronomy*, 6, 393
- Nimmo K., et al., 2023, *MNRAS*, 520, 2281
- Niu C. H., et al., 2022, *Nature*, 606, 873
- Oppermann N., Yu H.-R., Pen U.-L., 2018, *MNRAS*, 475, 5109
- Ould-Boukattine O. S., et al., 2022, *The Astronomer's Telegram*, 15817, 1
- Pearlman A. B., Majid W. A., Prince T. A., Kocz J., Horiuchi S., 2018, *ApJ*, 866, 160
- Perera B., et al., 2022, *The Astronomer's Telegram*, 15734, 1
- Petroff E., Hessels J. W. T., Lorimer D. R., 2022, *A&ARv*, 30, 2
- Pick M., Vilmer N., 2008, *A&ARv*, 16, 1
- Pleunis Z., et al., 2021, *ApJ*, 923, 1
- Rajwade K. M., et al., 2020, *MNRAS*, 495, 3551
- Rajwade K., et al., 2022, *The Astronomer's Telegram*, 15791, 1
- Ransom S. M., 2001, PhD thesis, Harvard University, Massachusetts
- Ravi V., 2022, *The Astronomer's Telegram*, 15693, 1
- Ravi V., et al., 2023, *ApJ*, 949, L3
- Serylak M., et al., 2009, *MNRAS*, 394, 295
- Seymour A., Michilli D., Pleunis Z., 2019, DM_phase: Algorithm for correcting dispersion of radio signals, Astrophysics Source Code Library, record ascl:1910.004 (ascl:1910.004)
- Sheikh S., et al., 2022, *The Astronomer's Telegram*, 15735, 1
- Snelders M. P., et al., 2023, *arXiv e-prints*, p. arXiv:2307.02303
- Sobacchi E., Lyubarsky Y., Beloborodov A. M., Sironi L., 2022, *MNRAS*, 511, 4766
- Sotomayor-Beltran C., et al., 2013, ionFR: Ionospheric Faraday rotation, Astrophysics Source Code Library, record ascl:1303.022 (ascl:1303.022)
- Spitler L. G., et al., 2016, *Nature*, 531, 202
- Suresh A., Cordes J. M., Chatterjee S., Gajjar V., Perez K. I., Siemion A. P. V., Price D. C., 2021, *ApJ*, 921, 101
- Sutinjo A. T., et al., 2023, *arXiv e-prints*, p. arXiv:2302.06220
- Tong H., Liu J., Wang H. G., Yan Z., 2022, *MNRAS*, 509, 5679
- Wada T., Ioka K., 2023, *MNRAS*, 519, 4094
- Wang P., et al., 2022, *The Astronomer's Telegram*, 15619, 1
- Whitney A., Kettenis M., Phillips C., Sekido M., 2010, in Navarro R., Rogstad S., Goodhart C. E., Sigman E., Soriano M., Wang D., White L. A., Jacobs C. S., eds, *Sixth International VLBI Service for Geodesy and Astronomy. Proceedings from the 2010 General Meeting*. pp 192–196
- Wild J. P., McCready L. L., 1950, *Australian Journal of Scientific Research A Physical Sciences*, 3, 387
- Wild J. P., Smerd S. F., Weiss A. A., 1963, *ARA&A*, 1, 291
- Wu Z.-W., et al., 2023, *arXiv e-prints*, p. arXiv:2304.14697
- Yan Z., et al., 2015, *ApJ*, 814, 5
- Zhang Y., et al., 2022, *The Astronomer's Telegram*, 15733, 1
- Zhang Y.-K., et al., 2023, *arXiv e-prints*, p. arXiv:2304.14665
- Zhou D. J., et al., 2022, *Research in Astronomy and Astrophysics*, 22, 124001
- van Straten W., 2006, *ApJ*, 642, 1004
- van Straten W., 2013, *ApJS*, 204, 13

van Straten W., Bailes M., 2011, *Publ. Astron. Soc. Australia*, 28, 1

APPENDIX A: DM DETERMINATION

In order to determine the DM we dedispersed the three brightest microshots in B1 and B2 to a range of DMs in the interval $219.2 - 219.55 \text{ pc cm}^{-3}$. The DM is then given by the centroid of a Gaussian fit to the sum of the S/N vs DM curves. These curves are shown in Figure A1. See the main text for more detail.

APPENDIX B: ACF ANALYSIS

In Figures B1 and B2 we show 2D ACFs of the bursts presented in this paper. See the main text and figure captions for more detail.

APPENDIX C: POLARISATION CALIBRATION

In Figure C1 we plot the polarisation fractions of our bursts as a function of frequency. A similar trend in Stokes V/I for all three bursts indicates a slight imperfection in the polarimetric calibration that does not, however, significantly influence our results or interpretation thereof.

This paper has been typeset from a \TeX/L\AA\TeX file prepared by the author.

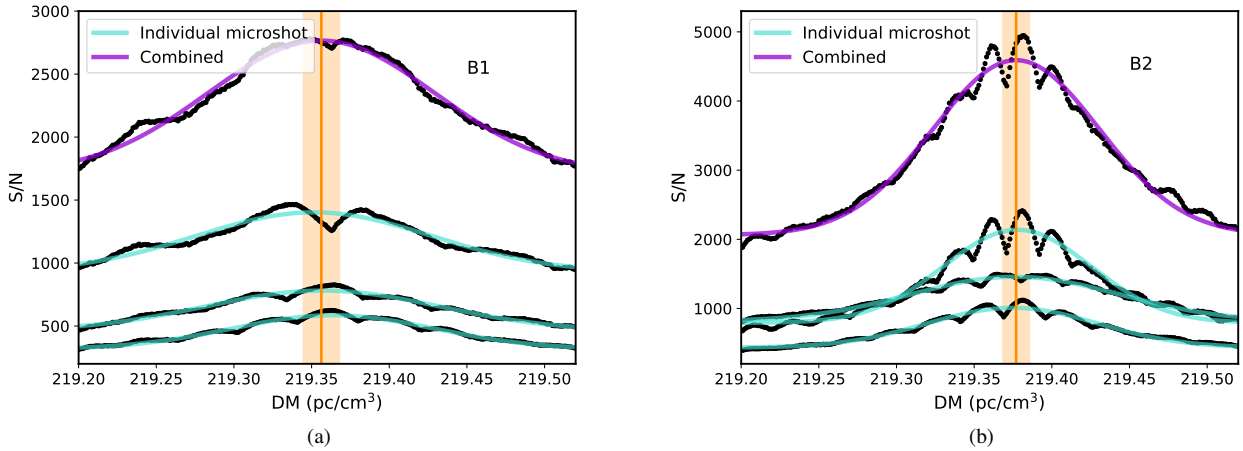


Figure A1. The S/N as a function of DM of the three brightest microshots in B1 and B2 are shown as black dots. Gaussian fits to these curves are overlotted in turquoise. The combined S/N of the three microshots is also shown, with a Gaussian fit in purple. The centroid of this Gaussian fit is indicated by the solid vertical orange line, while the shaded region shows the 3σ uncertainty. The scalloping in the curves is likely the result of the strongly scintillating microshots that have a duration comparable to the time resolution of our data.

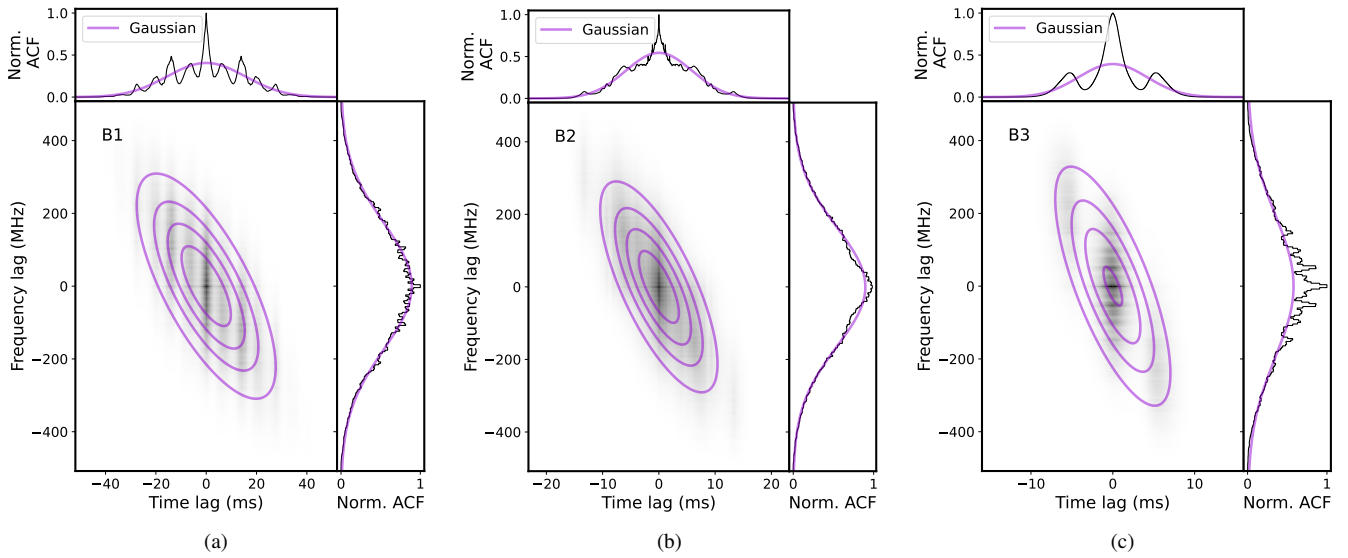


Figure B1. 2D autocorrelation functions of burst B1, B2, and B3 detected with the NRT. A 2D Gaussian is fitted to the 2D ACFs to determine the drift rate. The top panels show the 1D time ACF, while the right hand panels show the 1D frequency ACF. For more detail see the main text.

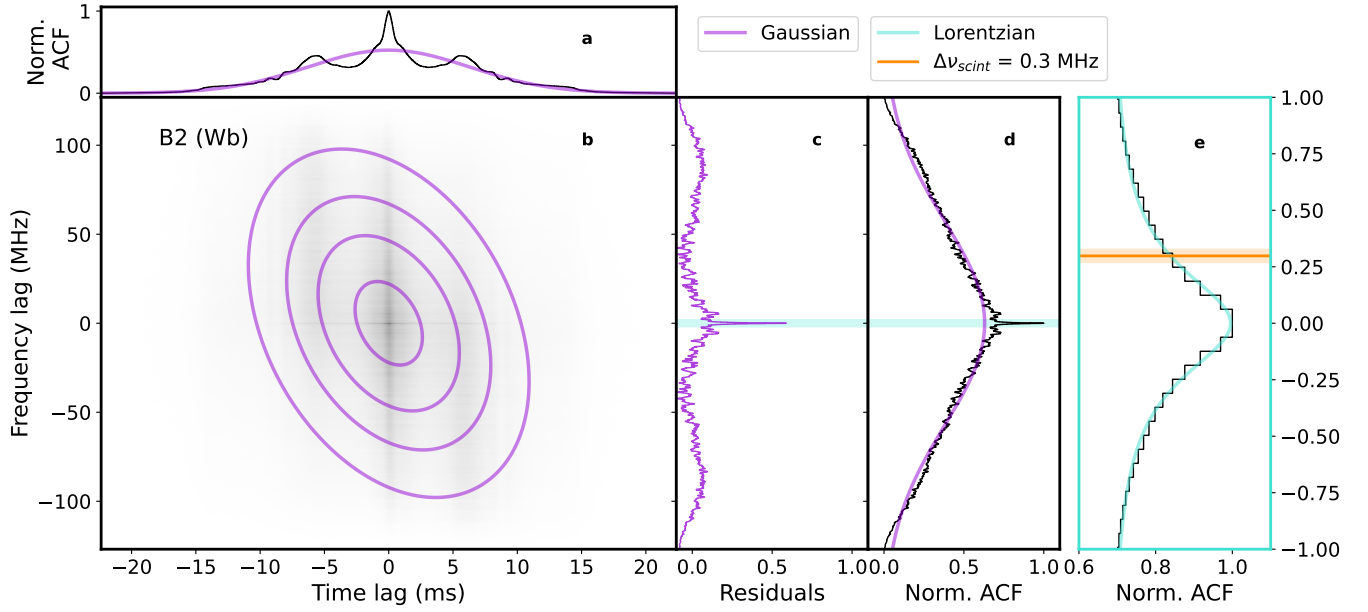


Figure B2. Panels a and c show 1D time and frequency ACFs, respectively, of B2 using the data from the Westerbork RT-1 dish. Gaussian fits have been overlotted in purple. Panel b shows the 2D ACF, with a 2D Gaussian fit overlotted in purple. The residuals of the frequency ACF as a fraction of the normalised maximum of the 1D ACF are shown in panel c. In panels c and d, a strong peak in the frequency ACF corresponding to the scintillation bandwidth has been highlighted in turquoise. Finally, we zoom in on this peak in panel e, where a Lorentzian fit is overlotted in turquoise. The HWHM of the Lorentzian function, which corresponds to the scintillation bandwidth, is indicated by the orange line, with the shaded orange regions showing the 3σ uncertainty. This value is consistent within a factor of 2 of the NE2001 prediction.

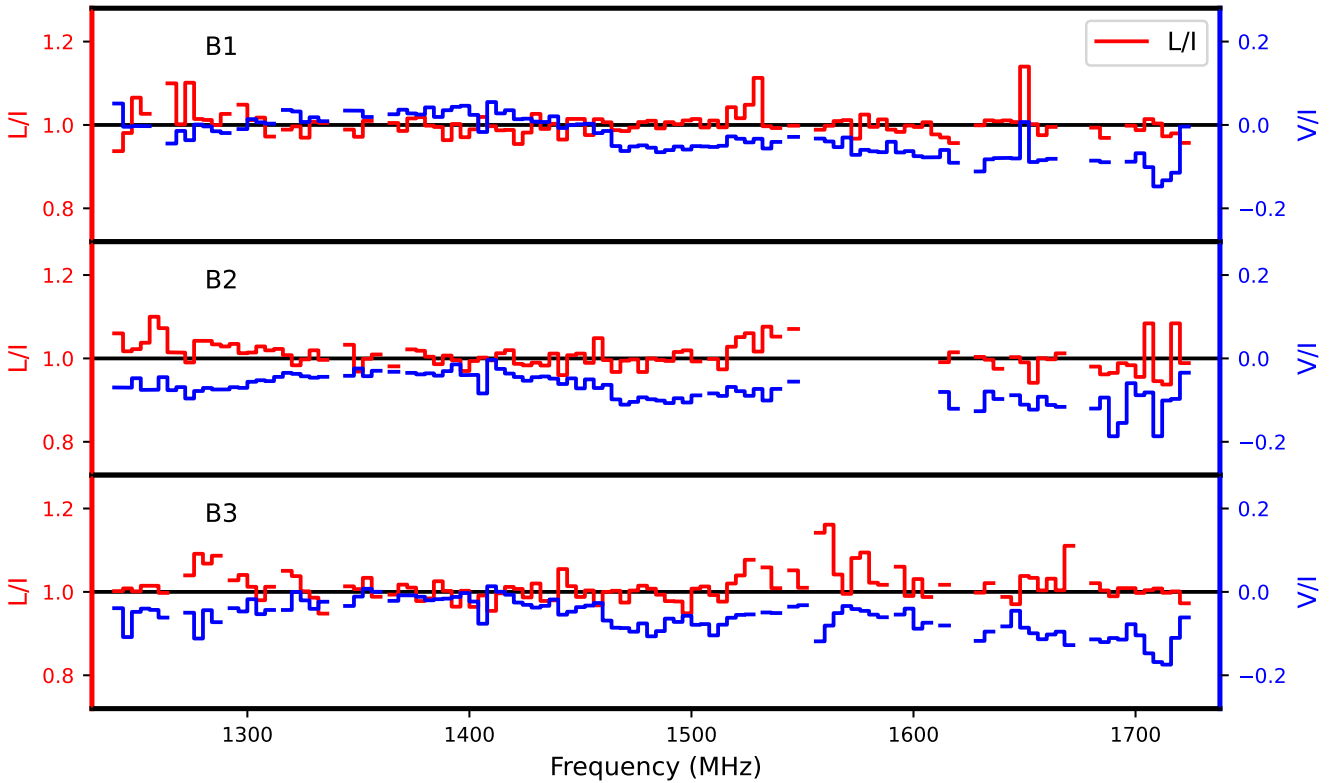


Figure C1. The linear (in red) and circular (in blue) polarisation fractions of B1, B2 and B3 as a function of frequency. Gaps occur due to channels that have been zapped to remove RFI contamination.